High-speed Intracellular Temperature Mapping Reveals the Existence of Non-Conductive Dissipation of Energy by Heating

Masaharu Takarada[1], Ryo Shirakashi[2], Masahiro Takinoue[3,4], Motohiko Ishida[1], Masamune Morita[3,5], Hiroyuki Noji[6], Kazuhito V. Tabata[4,6], Takashi Funatsu[1] and Kohki Okabe[1,4*]

[1]Graduate School of Pharmaceutical Sciences, The University of Tokyo, 7-3-1 Hongo, Bunkyo-ku, Tokyo 113-0033, Japan

[2]Institute of Industrial Science, the University of Tokyo, 4-6-1 Komaba Meguro-ku, Tokyo 153-8505, Japan

[3]Department of Computer Science, Tokyo Institute of Technology, 4259 Nagatsuta-cho, Midori-ku, Yokohama 226-8502, Japan

[4]JST, PRESTO, 4-8-1 Honcho, Kawaguchi, Saitama 332-0012, Japan

[5]Biomedical Research Institute, National Institute of Advanced Industrial Science and Technology (AIST), Center 6, 1-1-1 Higashi, Tsukuba, Ibaraki, 305-8566, Japan

[6]Graduate School of Engineering, The University of Tokyo, 7-3-1 Hongo, Bunkyo-ku, Tokyo 113-8656, Japan

*Correspondence should be addressed to: K.O. (okabe@mol.f.u-tokyo.ac.jp)

Abstract

Recently, intracellular thermometry has revealed temperature variations within cells. Although the biological significance of intracellular temperature change is recognized, the physical principles of intracellular temperature change remain a mystery. Here, we investigate intracellular heat transfer through intracellular temperature mapping using a fluorescent polymeric thermometer and high-speed fluorescence lifetime imaging microscopy. Through infrared laser irradiation assisted heating, we track changes in temperature distribution to examine the mechanism of intracellular heat dissipation in relation to heat conduction. Continuous heating provokes the significantly slower (second order) relaxation of averaged temperature of single cells compared to liposomes of comparable size, and is affected by intracellular structures and molecules. Furthermore, we reveal the existence of intracellular temperature relaxation independent of heat conduction. Our results may explain the mechanisms of temperature variation in cells that are unresolved based on our current understandings, providing the first step toward unraveling intracellular thermodynamics under non-equilibrium conditions.

Main

Temperature has a great influence on biological activity at various hierarchical levels. In cells, temperature is involved in cellular functions by controlling intracellular biochemical reactions. Recent advances in live-cell nano-thermometry, including our studies using a fluorescent polymeric thermometer (FPT)[1,2], have revealed temporal[3-7] and spatial[8-11] temperature changes in cells that are associated with cellular functions. On the basis of these findings, cellular intrinsic temperature changes are attracting attention in biology and medicine as a novel property that drives cellular activity and determines the cellular state[12-15].

It was proposed that the absolute amount of temperature change recorded in cells deviates significantly from the

value simply calculated by the heat conduction equation, where heat dissipates in a homogeneous aqueous solution[16]. This discrepancy (referred to as the 10^5 gap) has provoked discussions on the validity of methods for measuring intracellular temperature. Numerous reports[12,13] of intracellular temperature changes independent of the temperature-sensing strategies, including various light-independent methods, have now indicated that the 10^5 gap in temperature change is not due to errors associated with intracellular fluorescence thermometry. Therefore, the principles that give rise to these differences in intracellular temperature change remain a mystery.

To elucidate the principle of intracellular temperature change in relation to heat conduction, it is essential to observe the process by which such temperature change occurs, i.e., heat transfer in the intracellular space. This can be accomplished through capturing the temporal changes in the intracellular temperature distribution within the cell. However, currently available methods for the high-resolution measurement of intracellular temperature are limited to fast fixed-point local thermometry and snapshots of temperature distribution, thus it is difficult to track the intracellular temperature distribution at high speed.

In a previous study, we developed an accurate intracellular temperature mapping method using FPT and fluorescence lifetime imaging microscopy (FLIM)[2]. In this method, the fluorescence lifetime measurement enables accurate temperature imaging independent of the FPT concentration and excitation intensity. The use of fluorescence lifetime, in contrast to simple fluorescence intensity measurements, is a powerful strategy for visualizing temperature change in living organisms and cells because it does not depend on photobleaching, the movement and deformation of cells, and/or the effects of thermophoresis[17] during observation. However, because the determination of fluorescence lifetime requires a large number of photons, the spatiotemporal resolution in cellular thermometry is compromised. Therefore, intracellular temperature mapping provides only a snapshot of the temperature distribution, which barely shows the organelle-dependent temperature distribution even after 60 s of integration[2].

To determine the fluorescence lifetime at high speed, the fast fluorescence lifetime (hereafter referred to as fast lifetime) is suitable. Fast lifetime, defined by the average photon arrival time at each pixel, requires far fewer photons in fluorescence lifetime determination than the conventional approach[18] because it directly determines fluorescence lifetime values from photon recordings without a mathematical approximation. Determination of fluorescence lifetime by the conventional exponential approximation provides information about the photochemistry of fluorophores, which can be omitted in temperature measurements using the average fluorescence lifetime of FPT.

In this study, in addition to employing fast lifetime, we utilized the instrumentation for time-correlated single photon counting (TCSPC)-based FLIM, which has very high photon acquisition ability, to determine the fluorescence lifetime of FPT in local regions of cells in milliseconds without sacrificing temperature resolution. This high-speed FLIM with FPT allowed us to track intracellular temperature changes with high spatial and temporal resolution, namely, real-time temperature mapping. Next, we used the developed real-time temperature mapping method to track the transient temperature change caused by an artificial heat source in living cells and liposomes, revealing that the temperature relaxation in cells is slow and, moreover, that it is location- and molecule-dependent inside the cells. The detailed analysis of the intracellular temperature relaxation performed in relation to the heat conduction equation revealed that the intracellular temperature changes during continuous heating, similar to physiological thermogenesis, include temperature changes that do not depend on heat conduction. These results suggested that thermal energy remains localized without immediate dissipation, which controls thermal signaling in cellular functions.

Results

In this study, to explore the process of the change in temperature distribution within cells we adopted FPT (Figure 1a), which responds sensitively to temperature changes above the lower critical solution temperature (LCST) and can capture the temperature distribution in cells[2]. FLIM using the most accurate and pervasive TCSPC[18] was used for detecting the fluorescence lifetime of intracellular FPT.

First, we compared the fast lifetime and conventional fluorescence lifetime of FPT (Figure 1b, Supplementary Figure 1, and Supplementary Note 1). Figure 1c shows the relationship between the temperature of the cell medium and the fast lifetime of FPT in cells. The temperature resolution calculated from this temperature response curve was 0.14–1.5 °C (0.14–0.41 °C for 24–34 °C). Thus, the temperature response curve of FPT by fast lifetime was almost the same as that of the conventional method[2]. This difference in the fluorescence lifetime determination method also did not affect the temperature response curve using cell extract (Supplementary Figure 1). As the total number of photons increases, the variation of the calculated fluorescence lifetime value decreases, improving the accuracy of temperature measurement. We then evaluated the relationship between the number of accumulated photons and the standard deviation (s.d.) of conventional fluorescence lifetime and fast lifetime from a single cell (Figure 1d, Supplementary Figure 2). As shown in Figure 1d, the determination of the fluorescence lifetime of FPT by fast lifetime achieved similar accuracy with only 4% of photons compared to the conventional method.

Here, we performed intracellular temperature mapping with fast lifetime of FPT in living COS7 cells using the state-of-the-art FLIM having high photon acquisition capability (photon detection efficiency per unit time is 25 times higher than that of our previous system[2]). Comparing the fluorescence lifetime images at different measurement times, we found that the intracellular temperature mapping became more detailed in a time-dependent manner; the spatial heterogeneity of the intracellular temperature could be observed even at a measurement time of only 0.66 s, while a previous study[2] using FPT required a measurement time of 60 s (Figure 1e). The highly efficient fluorescence lifetime determination of this method enabled fluorescence lifetime imaging at high compartmentalization (e.g., 512 × 512 pixels). The results of high-resolution temperature mapping in a single COS7 cell (Figure 1f) clearly revealed a heterogeneous temperature distribution not only at the organelle level, such as a high temperature in the nucleus, but also in micro-spaces in the cytoplasm and nucleoplasm. When the heterogeneous temperature distribution visualized in an intracellular micro-space was compared with that in a homogeneous aqueous solution of the same size, the spatial fluctuation of the intracellular temperature was notably large (Figure 1g). Next, mapping of the temperature distribution was performed in a cell in which mitochondria, the main heat-generating organelles in the cell, were visualized (Figure 1h). As in our previous study[2], the mitochondria were clearly shown to have a higher temperature (ΔT = 1.29 °C) than the surrounding region in steady-state cells.

Next, to observe the change in intracellular temperature with this mapping method, we heated an intracellular local area via infrared (IR) laser (1480 nm) irradiation as an artificial heat source. By directly stimulating the O-H vibration of water molecules, an irradiating IR laser focused on a glass surface (Figure 2a) can heat up an aqueous solution in a local area (1 μm in diameter) in a transient and power-dependent manner[19,20]. Considering that the fluorescence lifetime values and the components of the fluorophore [7-(*N*,*N*-dimethylaminosulfonyl)-2,1,3-benzoxadiazol-4-yl, DBD] in FPT are sensitive to the chemical environment (e.g., hydrophobicity)[21], we confirmed that the irradiation-

dependent increase of fast lifetime was due to the temperature change by analyzing the details of the fluorescence decay curve of FPT at the heating center in the nucleus and the cytoplasm. As shown in Supplementary Figure 3, an increase in intracellular local temperature was verified by the concordance of the fluorescence decay curves (i.e., the fluorescence lifetimes and their compositions of the two components) during IR laser heating and medium heating. These results confirm that the FPT response was independent of the chemical environment upon heating by IR laser irradiation. Figure 2b shows the results of fluorescence lifetime imaging in the cells under IR laser irradiation, demonstrating the concentric distribution of temperature around the point of IR laser irradiation. When the nucleus was irradiated with the IR laser, the temperature gradient formed in the nucleus was steeper than that in the cytoplasm, even though the amount of heat applied to the nucleus and the cytoplasm was the same (Supplementary Figure 4). Next, the increase in intracellular averaged temperature upon IR laser irradiation was dependent on the laser intensity (Figure 2c). To investigate the reliability of intracellular temperature change recorded during this artificial heating, we examined the results using another fluorescent thermometer with a completely different temperature response principle. Rhodamine B has long been known for the high temperature dependence of its fluorescence quantum yield[22] and has been used to measure solution temperature in nanoscale space[23]. Although the fluorescence intensity-based measurement of temperature cannot be used for intracellular temperature mapping or observation of local temperature changes due to local fluorophore concentration change, it can be used to track the average temperature of the entire cell. Here, we quantitatively investigated the intracellular temperature change during IR laser irradiation using the temperature-dependent change in fluorescence intensity of intracellular Rhodamine B-labeled dextran (molecular weight 10,000) (Supplementary Figure 5). The results showed that the change in averaged temperature during IR laser heating was the same between the two methods, which confirmed the validity of the temperature change measurement by fast lifetime of FPT. In addition, by repeating the temperature mapping upon transient intracellular heating with an IR laser, we examined the ability to track the intracellular temperature distribution using this method. As shown in Figure 2d, the increase in fluorescence lifetime upon IR laser irradiation returned to the pre-irradiation value when the irradiation was stopped, and the temperature gradient could be repeatedly formed. Lastly, we quantitatively verified the temporal and spatial resolution of this temperature measurement using an artificially temperature-manipulatable IR laser, and determined that they are 9 ms and at the diffraction limited level, respectively (Supplementary Figures 6 and 7, Supplementary Note 2).

By taking advantage of the high temporal resolution of this high-speed temperature mapping method (9 ms), we observed the time-course of temperature changes in cells. Here, the average temperature of a finite region containing the heat source was analyzed. This average temperature change represents the change in the thermal energy of this region, divided by the heat capacity. First, the changes in averaged temperature of whole cells during pulsed and continuous heating are shown in Figure 3a. The results of fast rise and fast relaxation of temperature change during pulsed heating confirm that our high-speed temperature mapping method is useful for tracking fast intracellular temperature change of several tens of milliseconds. The temperature relaxation during pulsed heating was consistent with the time resolution limit of the present temperature tracking method (Supplementary Figure 6, Supplementary Note 2). In the case of continuous heating, the temperature rapidly increased followed by a gradual increase upon IR laser irradiation, and then gradually decreased upon stopping the irradiation (Figure 3a). Because the relaxation rate did not depend on the magnitude of the temperature rise (Supplementary Figure 8), we normalized the temperature

change and compared the curves of relaxation, finding that the relaxation after stopping continuous heating was slower than that in the case of pulse heating. As shown in Supplementary Note 3, the relaxation of the average whole-cell temperature during this continuous heating exhibited two-component time constants on the order of seconds. We also tracked the average temperature of whole cells using Rhodamine B. As shown in Supplementary Figure 9, the slow intracellular temperature relaxation after continuous heating shown by Rhodamine B was in excellent agreement with the results obtained by FPT. In addition, we confirmed the slow intracellular temperature relaxation using Cy3 tagged by Streptavidin (Supplementary Figure 10). These results show that this slow temperature relaxation upon continuous heating was an intrinsic cellular property. Further investigation of the heating duration dependence of the intracellular relaxation rate revealed that it slows down in a heating duration-dependent manner and gradually saturates after heating for more than 5–10 seconds (Supplementary Figure 11).

Tracking the temperature of local areas in cells can help us understand the principles that determine the organelle-specific temperature variation within them. Thus, we conducted temperature tracking of micro-spaces of cells. By following the changes in fluorescence lifetime in local regions of cells, we were able to track the changes in average temperature of finite region (a square area of 10 μm per side with vertical thickness of z-resolution in this imaging method) with a time resolution of several tens of milliseconds, and we observed the continuous heating-dependent slow temperature relaxation even in the local cytoplasm (Figure 3b). Therefore, we compared the temperature relaxation in different locations in cells. We monitored the temperature in the nucleus when heated; as shown in Figure 3c, the relaxation of averaged temperature in the nucleus was slower than that in the cytoplasm. This slow nuclear temperature relaxation may be partly due to nuclear-specific transcription and RNA content, because transcription inhibition accelerated nuclear temperature relaxation (Supplementary Figure 12). Furthermore, the rate of temperature relaxation in small spaces can be measured in giant plasma membrane vesicles (GPMVs) of 10 μm diameter directly isolated from living cells, which was significantly faster than a region of similar size in the cytoplasm (Supplementary Figure 13).

To compare the results of slow temperature relaxation obtained in cells with a volume of water of the same size, we next attempted to track the temperature variations of liposome, a micrometer-sized artificial compartment with a lipid bilayer (Supplementary Figure 14 and Supplementary Video 1). The comparison of the relaxation of averaged temperature after continuous heating of liposomes with that in an intracellular local space of the same size clearly showed that the temperature relaxation in water was faster than that observed in single living cells (Figure 3d). These results suggest that the slow temperature relaxation observed in cells is an intracellular component-dependent phenomenon.

Here, the time of temperature relaxation observed in cells after continuous heating (Figure 3b−d) was compared with numerical calculations based on heat conduction. Numerical calculations based on the unsteady heat conduction equation, which consists of only a simple thermal diffusion term, using the thermal conductivity and specific heat of cell showed that the time required for the relaxation of averaged temperature in cell by heat conduction is on the order of ms (Supplementary Figure 15 and Supplementary Note 4). This comparison with the numerical calculation shows that the relaxation of averaged temperature upon continuous heating observed in cells (which occurs on the order of seconds) is much slower than that by heat conduction.

Owing to the non-negligible difference in the relaxation time, we examined whether the intracellular temperature

variation originates from heat conduction. Given the diffusive nature of heat, the temperature distribution immediately before the cessation of heating is essential for understanding the mechanism of temperature relaxation. For this purpose, we constructed a method to track the intracellular temperature distribution during heating and relaxation. Because the temperature mapping with high temporal resolution severely limits the number of photons per pixel, we employed repeated measurements to achieve temperature distribution tracking in single cells (Figure 4a, Supplementary Figure 16 and Supplementary Video 2), by taking advantage of the long-time measurement capability of this method (photobleaching-independence of fast lifetime) and the property of our thermal measurements where the temperature returned to its initial state. Using this method, we investigated whether the characteristic dependency of the relaxation of intracellular averaged temperature relaxation on the heating durations shown in Figures 3a, 3b and S11 are attributable to heat conduction.

According to the heat conduction equation, where thermal properties remains constant and there are no exothermic or endothermic sources, the rate at which the average temperature relaxes after heating stops is determined by the temperature distribution in the initial condition (Supplementary Note 5). Therefore, we investigated whether the average intracellular temperature relaxation rate, as observed in Figure 3, depends on the initial temperature distribution. As shown in Figure 4b, the average temperature relaxation rate was directly compared under the condition that the temperature distribution was kept constant immediately before heating was stopped (i.e., the initial condition), regardless of the heating time. This was achieved by adjusting the IR laser intensity. The results showed that the average temperature relaxation rate of the whole cell was slower with longer heating times, despite almost identical initial temperature distributions (Figure 4c and Supplementary Movies 3–5). These results suggest that the rate of intracellular temperature relaxation is not determined by the initial temperature distribution; however, it is influenced by the heating duration, indicating that the intracellular temperature relaxation rate cannot be explained by heat conduction alone.

The results were then also verified with respect to the diffusive nature of heat transfer in heat conduction. If heat transport only occurs via conduction, the heat quantity decreases because of conduction from the region's boundary; therefore, for the same temperature distribution, the time constant for the average temperature relaxation rate depends on the size of the region. By using the equation (S3 and Supplementary Note 4) of heat conduction, we numerically calculated and compared the average temperature relaxation rate of various areas (D = 3, 5, and 10 μm, where D is diameter). The calculated relaxation time of the average temperature in the finite region containing the heat source was found to increase with an increase in the region size (Figure 4d). We also investigated the intracellular relaxation rate of the area-averaged temperature for observation areas of varying sizes centered on the heat source (L = 3, 5, and 10 μm, where L is length of one side of the square area). In contrast to the numerical calculation based on heat conduction, the relaxation rate of the area-averaged temperature observed in the cells exhibited negligible dependence on the area size (Figure 4e). The clear difference in the size dependence of the temperature relaxation rate between simulations based on the heat conduction equation and observations in living COS7 cells (Figure 4f) indicates that intracellular heat dissipation does not depend solely on heat conduction. Therefore, it is suggested that, in addition to heat conduction, exothermic and endothermic processes contribute to the intracellular heat transport pathway.

Finally, to investigate the cause of the slow temperature relaxation in cells, we attempted to directly observe the slow relaxation of temperature gradient in the intracellular micro-space. Figure 5a and 5b show the tracking of the

temperature distribution of local areas when stopping IR laser irradiation. In both the cytoplasm (Figure 5a and Supplementary Video 6) and the nucleus (Figure 5b and Supplementary Video 7), the temperature gradient was maintained around the heating point for approximately 200 ms (cytoplasm) and over 300 ms (nucleus) after the heat source disappeared. In addition to this, the temperature relaxation of the entire field of view was observed on the order of seconds. The temperature relaxation in the localized regions in the nucleus was slower than that in the cytoplasm (Figure 5a,b), which is consistent with the findings on the tracking of average cell temperature shown in Figure 3. Furthermore, the difference in temperature relaxation in these two areas was clearly confirmed by the difference in the relaxation rate of the temperature gradient when heating was performed on the nuclear membrane (Supplementary Figure 17). These results indicate that slow heat transport in the intracellular microspace contributes to the slow temperature relaxation in cells.

Discussion

In this study, we developed a high-speed temperature mapping method in cells through FPT and ultrasensitive FLIM. Using this method, we revealed that the measured average intracellular temperature slowly relaxes, which was in contrast to the rapid relaxation of the average temperature in liposomes containing homogeneous aqueous solutions. Furthermore, by taking advantage of the high spatiotemporal resolution of this temperature mapping, we found that temperature relaxation depends on the intracellular location. We concluded that this significantly slower temperature relaxation measured inside cells compared to a homogeneous aqueous solution when cells were continuously heated is an intrinsic property of cells, and is not due to undesirable side effects of FPT, based on examinations of various heating (Figures 3a, 3b, and Supplementary Figure 5) and measurement method (Supplementary Figure 9). The feasibility of the fast temperature mapping method with FPT and the slow intracellular temperature relaxation upon continuous heating were confirmed in the investigations in another mammalian cell line using HeLa cells (Supplementary Figure 18).

Compared with a previous study[2], the present study significantly enhances the spatial and temporal resolution of intracellular temperature mapping. This method enabled real-time temperature mapping with a temporal resolution of 41 ms at high spatial resolution, revealing organelle-specific temperature distributions in cells. If the photon budget is devoted only to spatial or temporal resolution, temperature mapping with high compartmentalization (512 × 512 pixels) and rapid temperature measurement times (9 ms) are possible (Supplementary Note 2). Through this high-speed temperature mapping, we observed—for the first time—the relaxation process of the intracellular temperature distribution upon local heating. This phenomenon was difficult to observe by conventional intracellular thermometry methods[11,12], such as intracellular fixed-point thermometry using fluorescent nanoparticles (nanodiamonds, quantum dots, and up-conversion nanoparticles) and temperature tracking in specific organelles using small fluorescent molecules and proteins.

By observing in situ heat transfer locally inside cells, we revealed that continuous heating provoked a slow temperature relaxation (Figure 3, Supplementary Figure 14, Supplementary Figure 18c, and Supplementary Note 3 and 4) and this temperature relaxation process does not follow the heat conduction equation with only a diffusion term (Figures 4b and 4c). This finding suggests that intracellular temperature changes are accompanied by heat transport processes involving energy conversion in addition to heat conduction. Therefore, we reconsidered the

energy dissipation process in cells during continuous heating. The average temperature relaxation rate in the intracellular region depends on intracellular organelles (such as the nucleus), RNA (Supplementary Figure 12), and structures and large molecules that do not enter the GPMV (Supplementary Figure 13). In addition, we observed that both heat dissipation from the inside to the outside of the cell and heat transfer in the intracellular space were slow (Figures 5a and 5b). From these results, we speculate that the thermal energy generated by the absorption of infrared laser light by intracellular water and biomolecules is propagated through energy absorption associated with state changes of specific molecules (related to the above structures) in the neighborhood, in addition to being dissipated by heat conduction. This phenomenon may be attributed to the longer (and thus non-negligible) molecular relaxation times of high energy states of molecules (e.g., higher-order structures) induced by continuous heating compared with the relaxation times caused by heat conduction. For instance, the intrinsic relaxation times of RNAs depend on their interactions[25]. When these relaxation times are longer than the relaxation time caused by heat conduction (on the order of ms, see Supplementary Note 4), we can assume that the molecular relaxation of RNAs is the kinetic rate-limiting step in thermal dissipation. As a result, this molecular relaxation dominates the thermal dissipation of both RNAs and molecules that can share energy with RNAs. The thermal excitation of these biopolymers, along with the resulting energy conversion, keeps them in a higher energy state. However, considering that measurements with different temperature probe molecules—which are expected to have distinct affinities to biomolecules, varying temperature-sensing chemistry, and different molecular relaxation times—recorded the same intracellular heat dissipation rates (Supplementary Figures 9 and 10) and intracellular temperature changes on the same order[1-13,15], it is unlikely that molecular relaxation of the probe molecules affects the measurement of intracellular temperature. As similar temperature measurements can be made regardless of the type of thermometer, the implication is that energy is shared among biopolymers, which each possess unique dynamics.

On the other hand, an equilibrium system also exists within the cell in which heat is dissipated by conduction. In fact, our pulsed heating experiments and the recently developed temperature measurement by refractive index change showed a fast temperature relaxation and a thermal conductivity not much different from that of water[24]. These facts suggest that intracellular temperature change includes both the temperature defined by a group of biomolecules under non-equilibrium conditions and the temperature governed by the heat conduction equation which relies solely on thermal diffusivity. Examples of such non-equilibrium relationships between systems with different mechanisms of heat transfer (i.e., different temperature-determining populations) can be found in plasmas (electrons and cations)[26] and metal crystals (free electrons and phonons)[27]. In these examples, as the rate of energy conversion between systems in non-equilibrium states is not determined by the thermal conductivity of each system, it is possible to define different temperatures for the two systems within a time shorter than the relaxation time of that energy conversion. In cells, because of the energy conversion of certain biomolecules through state changes and their subsequent relaxation, resulting in low heat transfer rates, it is possible to define different temperatures within the two systems within the time required for energy dissipation. The elucidation of the specific mechanisms of energy conversion and molecular relaxation of biomolecules that generate this hypothetical temperature difference between the two systems may lead to an accurate definition of the intracellular temperature, encompassing non-equilibrium conditions—an area that requires further exploration in future thermodynamic investigations.

To understand heat transport in biological samples of various sizes, such as cells, tissues, and organs, it is necessary

to consider the spatial scale of the observations. The time required for the temperature variations within the entire system to disappear via heat conduction strongly depends on the size of the space. On the other hand, as biological macromolecules have unique conformational change timescales that depend on their structure[25], the relaxation times of thermally excited molecules are independent of the size of the space. Therefore, the time required for heat dissipation via heat conduction in certain space sizes (i.e., in large spaces) is non-negligible compared with the relaxation time of the molecules. The relaxation time of subcutaneous tissue temperature observed in mice using a luminescent nanothermometer showed little deviation from the heat conduction model[28]. The phenomenon revealed in this study, i.e., that the intracellular temperature change is not completely governed by heat conduction, is observed only in the single-cell space. This suggests that, specially in cells, it is inappropriate to assume that all thermal energy is dissipated via heat conduction when determining the thermal conductivity and other thermal properties from temperature changes, given the non-negligible effects of energy conversion and molecular relaxation of biomolecules. The cellular thermal conductivity recently estimated from the steady-state temperature change of nanoparticles[29] differed significantly from the intracellular thermal conductivity determined from the equilibrium thermal measurement[24]. This may be due to non-negligible molecular relaxation at the single cell scale in the former method.

Until now, the physical mechanism causing the discrepancy (10^5 gap) between the temperature change inside the cell and the temperature change calculated by the heat conduction equation of a homogeneous system was unknown. The discovery of the existence of a very slow heat transport process that is independent of conduction highlights a critical flaw in attempts to estimate the temperature change during spontaneous intracellular heat generation from the thermal conductivity and the heat conduction equation. In particular, regarding the large discrepancy of 10^5, our findings challenge the basic assumption that intracellular temperature changes are caused solely by simple heat conduction. Slow intracellular heat transport discovered in this study (Figure 4), which cannot be described by the simple heat conduction equation, can explain the temperature change during intracellular heat generation that lasts for more than 1 s. In fact, cells with slower heat dissipation had a greater temperature increase during endogenous heat generation (i.e., mitochondrial stimulation) (Supplementary Figure 19). In addition, we estimate an intracellular temperature increase of 1.1 °C when heat dissipates independent of conduction (i.e., the cell can be assumed to be adiabatic homogeneous) upon mitochondrial stimulation (Supplementary Note 6). This temperature increase is in excellent agreement with the intracellular temperature increase measured in both the present (Supplementary Figure 19) and previous studies[12,13]. This consistency demonstrates the importance of considering the thermal excitation of intracellular biopolymers and their energy dissipation processes, rather than relying solely on simple heat conduction equations when attempting to understand the mechanism of intracellular temperature change.

Furthermore, the temperature elevation of biomolecules (which can be sensed by molecular thermometers) induced via slow intracellular heat dissipation has physiological significance. The slow heat transfer during continuous artificial heating observed in this study is also expected to occur during relatively long-term (on the order of minutes) physiological heating within the cell, such as mitochondrial heating (Supplementary Figure 19). One study has reported that spontaneous heat generation, which was dependent on the activity of the neuron, caused an intracellular temperature rise (ΔT = 2.12 °C), activating its own thermosensitive Transient Receptor Potential Vanilloid 4 (TRPV4)[30]. More recently, a thermal signaling mechanism has been discovered in neuronal cells where spontaneous temperature increase (ΔT = 0.9 °C) in the nucleus has a positive effect on important developmental processes during

neuronal differentiation[31]. The slow intracellular energy relaxation could explain how heat generated at the single-cell level contributes to these thermal signaling mechanisms, which are activated by the aforementioned high temperatures. Thus, slow heat dissipation in cells may play a pivotal role in facilitating the temperature rises that trigger various physiological cellular functions[15,30,31].

This method satisfies the temperature and time resolution levels[12] required in the study of recently emerging thermal medicine and thermal biology with spontaneous temperature fluctuations of the order of a few seconds at the lowest. Tracking of intracellular temperature distribution in fast medical phenomena (e.g., epilepsy[32,33], cancer hyperthermia[34], and imflammation[35]) and cell biological events (body temperature control by brown adipose tissue[12,13], embryogenesis[36,37], neuronal activity[30,31,38], apoptosis[1], and liquid-liquid phase separation[39]) should contribute to clarifying the mechanisms behind these phenomena. Furthermore, such temperature measurement studies on various physiological phenomena should contribute not only to the understanding of intracellular temperature variations and their molecular mechanisms, but also to the discovery of new forces driving cellular functions where energy is used by molecules in cells[15], which can be predicted from the slow energy relaxation found in this study. Through these investigations, the high-resolution temperature mapping method established here should provide novel findings on cellular biology.

Methods

Cell culture

COS7 cells and HeLa cells (Riken, Wako, Japan) were cultured in Dulbecco's Modified Eagle's Medium (DMEM) with 10% fetal bovine serum supplemented with penicillin–streptomycin, L-glutamine, sodium pyruvate, and nonessential amino acids at 37 °C in 5% CO_2. For live-cell imaging, cells were cultured in 35-mm glass-bottomed dishes (AGC Techno Glass, Shizuoka, Japan) and the medium was replaced by phenol red-free culture medium containing HEPES buffer (2 mL) before live-cell imaging. All solutions were from Thermo Fisher Scientific (MA, USA).

Microinjection into living cells and culturing on the microscope

Microinjection of FPT[2], Rhodamine B-labeled dextran (molecular weight 10,000; Thermo Fisher Scientific), and Cy3 tagged Streptavidin (FUJIFILM Wako Pure Chemical Corporation, Osaka, Japan) into living cells was performed with Femtojet (Eppendorf, Hamburg, Germany), controlled by a micromanipulator (Eppendorf). FPT (0.5 w/v%), Rhodamine B-labeled dextran (20 μM), and Cy3 tagged Streptavidin (3 μM) were dissolved in an aqueous solution containing 140 mM KCl, 10 mM KH_2PO_4–K_2HPO_4, and 4 mM NaCl. The solution was filtered using an Ultrafree-MC filter (Merck Millipore, MA, USA) and microinjected into the cytoplasm with a glass capillary needle (Femtotips II; Eppendorf). The volume of injected solution was estimated to be 2 fL.

The temperature of the culture medium was maintained at 26 °C for monitoring temperature change and at 24 °C for imaging temperature distribution. We chose these temperatures because they are the temperatures associated with the highest sensitivity for measuring temperature with FPT (see Figure 1c) in each experiment. The temperature of the culture medium was controlled and monitored with a stage-top incubator and a microscope objective lens heater (INUBSF-ZILCS; Tokai Hit, Fujinomiya, Japan).

Preparation of cell extract

The COS7 cell pellets were collected and resuspended in a buffer (30 mM HEPES (pH 7.4), 75 mM Sucrose, 225 mM Mannitol, 0.1 mM EGTA). After the addition of protease inhibitor cocktail (EDTA-free, Nacalai Tesque, Inc, Kyoto, Japan), the cell suspend was lysed using Dounce Tissue Grinder (Wheaton, Millville, NJ), followed by the three times of centrifugation (600 g, 10 min, 4 °C). Following further centrifugation (10,000 g, 10 min, 4 °C) of the supernatant, KCl was added to make the ionic strength 0.3 M. The concentration of proteins in the obtained cell extract was quantified with BCA Protein Assay Kit (Thermo Fisher Scientific) after treated with 1% Triton X-100 (Sigma-Aldrich, Burlington, MA) to be 2.9 $mgmL^{-1}$.

Fluorescence lifetime imaging of living cells, cell extracts and GPMVs

Time-correlated single-photon counting (TCSPC)-based fluorescence lifetime imaging microscopy (FLIM) was performed on a TCS SP8-FALCON confocal laser-scanning microscope (Leica Microsystems) with a pulsed diode laser (PDL 800-B, 470 nm; PicoQuant, Berlin, Germany) at a repetition rate of 20 MHz, and the emission from 500 to 640 nm was obtained through the described objective with 1–18.2 zoom factors and a binning procedure (factor: 1 or 2) in a 64×64–1024×1024-pixel format for 0.7–257.5 s. To obtain the conventional fluorescence lifetime (τ_f), the fluorescence decay curves of FPT in single cells and cell extract were fitted with a double exponential function, as previously reported[2]. The temperature response curves for the temperature mapping with FPT in single cells and cell extract were obtained by approximating the relationship between the averaged fast fluorescence lifetime (τ_{FAST}) of FPT (in triplicate) and the temperature to the fifth- or sixth-degree polynomials (coefficients of determination for both $R^2 = 0.999$):

$$\tau_{\text{FAST, living COS7 cell}}(T) = 0.0603644272864967T^5 - 2.27554925190688T^4 + 34.1786499772982T^3 - 255.3666687T^2 + 949.582685485572T - 1381.94789212487 \quad (1)$$

$$\tau_{\text{FAST, COS7 cell extract}}(T) = -0.0000046669T^6 + 0.0008623426T^5 - 0.0654657569T^4 + 2.6100824804T^3 - 57.5778063053T^2 + 666.2704802512T - 3157.2782188756 \quad (2)$$

$$\tau_{\text{FAST, living HeLa cell}}(T) = 0.0504967104200471T^6 - 2.26638446940322T^5 + 42.0594063916615T^4 - 412.714691229774T^3 + 2256.40968069216T^2 - 6509.58277053094T + 7755.40769741854 \quad (3)$$

where T and $\tau_{FAST}(T)$ represent the temperature (°C) and the fast fluorescence lifetime (ns) at T °C, respectively. The temperature resolution of this thermometric method using FPT was evaluated as previously reported[2]. The determined variation in temperature distribution [calculated from the s.d. of τ_{FAST} in the left panel (solution) of Figure 1g] derived from the acquisition of the fluorescence lifetime distribution was at the same level as the aforementioned temperature resolution.

Fluorescence imaging of the cells

Confocal fluorescence imaging was performed on a TCS SP8-FALCON confocal laser-scanning microscope (Leica Microsystems, Wetzeler, Germany) with a laser (638 nm) and an HC PL APO 63×/1.40 Oil CS2 objective (Leica Microsystems). Mitochondria and the nucleus were labeled with MitoTracker Deep Red FM (Thermo Fisher Scientific) and SiR-DNA (Cytoskeleton, Inc., CO, USA), respectively, and the fluorescence from 650 to 750 nm was obtained.

Confocal fluorescence imaging of Rhodamine B and Cy3 were performed on a TCS SP8-FALCON confocal laser-scanning microscope (Leica Microsystems) with a laser (552 nm and 488 nm), and the fluorescence from 560 to 700 nm and 500 to 700 nm were obtained, respectively.

Monitoring transient heating with IR laser irradiation

An IR laser (FRL-DC 1480 nm, maximum power, 3 W; IRE-Polus, MA, USA) was installed in a TCS SP8-FALCON confocal laser-scanning microscope (Leica Microsystems) through the IR-LEGO system (Sigma Koki, Tokyo, Japan) for the local heating of living cells and liposome, as shown in Figure 2a. An HC PL APO 63× 1.40 N.A. OIL CS2 objective (Leica Microsystems) was used to focus the IR laser and image the fluorescence lifetime of specimens; the diameter of the focused area in the IR laser irradiation was estimated to be 1.29 μm. An electronically controlled shutter (SSH-C4B; Sigma Koki) was used to start and stop the irradiation of the IR laser. The durations of irradiation were 0.1–5 s. The timing of stopping heating was analytically determined by the rapid drop in FPT fluorescence intensity. Considering that the heating operation using the shutter and the timing of the scanning in imaging are not perfectly synchronized, the first frame after the fluorescence lifetime drop was excluded because it may not reflect the temperature.

Tracking structural transition of FPT

The response time (τ) of the thermometers was determined by approximating with a single exponential function:

$$F(t) = a \exp(-t/\tau) + b \qquad (4)$$

where $F(t)$ and t represent the fluorescence intensity and time (s), respectively, and a and b are constants.

Fluorescence recovery after photobleaching (FRAP) analysis of FPT in living COS7 cells

The mobility of FPT in living cells was investigated by fluorescence recovery after photobleaching (FRAP). In the FRAP experiments, a small round area in living COS7 cells microinjected with FPT was photobleached for 2 s with 488 nm laser light focused on the area in the cytoplasm, followed by time-lapse confocal fluorescence imaging (described in Methods) over 200 s. In the image analysis, the fluorescence recovery was determined using the ratio of the averaged fluorescence intensity of the photobleached spot area to that of the whole cytoplasm calculated for each time point. The time course of fluorescence recovery for FRAP employing a uniform circular beam was fitted using the formula of Soumpasis *et al.*[40].

Preparation of giant plasma membrane vesicles (GPMVs)

COS7 cells injected with FPT were washed twice, then incubated with PFA and DTT dissolved in buffer (10 mM HEPES (pH 7.4), 150 mM NaCl, 2 mM $CaCl_2$) for 3 hours at room temperature.

Preparation and fluorescence imaging of liposome

Briefly, 1,2-Dioleoyl-sn-glycero-3-phosphocholine (DOPC) was dissolved in chloroform/methanol mixtures (2/1, v/v). Then, 20 μL of DOPC solution (2 mM) was poured into a glass test tube and gently dried using a flow of air to produce a thin DOPC film at the bottom of the glass tube. This DOPC film was subsequently dried under a vacuum for 2 h. It was then hydrated with 190 μL of Rhodamine B- labeled dextran (10 μM) in a 200 mM sucrose solution at 50°C overnight after 5 min of prehydration (50°C) using 10 μL of the solution. The final DOPC concentration was 0.2 mM.

To prevent liposomes from moving out of the field of view upon IR laser irradiation due to convection, a microsized chamber array[41] of 20 μm in diameter and 50 μm in depth was introduced and a single liposome was placed in the well. First, a cover slip, on which microchambers were fabricated with SU-8, was treated with 2 μL of 200 mM glucose solution and deaeration, followed by the application of 18 μL of the solution containing liposomes. Then, this cover slip with microchambers was sealed with a cover glass to allow fluorescence lifetime imaging.

Confocal fluorescence imaging of liposomes was performed on a TCS SP8-FALCON confocal laser scanning microscope (Leica Microsystems), as described above. The fluorescence signal observed inside the liposome using confocal microscopy confirmed the inclusion of Rhodamine B-labeled dextran. Temperature changes were determined from the temperature-dependent fluorescence intensity of Rhodamine B in aqueous solution (Fluorescence intensity = $1.8294e^{-0.0229T}$, where T indicates the temperature; $R^2 = 0.99$).

Comparison of the time-course of temperature relaxation

The time-course of the temperature relaxation normalized by the temperature increase just before cessation of the heating by IR laser irradiation was analyzed. The line of fitting with an exponential function is shown for reference. The area under the curve (AUC) of normalized temperature relaxation for 3.5 s was also calculated, followed by statistical analysis. The first two points were excluded in the calculation of AUC because the time required for the structural relaxation of FPT does not reflect the temperature (Supplementary Figure 6).

Treatment with Actinomycin D

The chemical stimulus was conducted by adding 2 μgmL^{-1} Actinomycin D (Nacalai Tesque, Inc., Kyoto, Japan) to the culture medium 6 h prior to the observation.

Tracking of intracellular temperature distribution upon IR laser heating

Because the temperature mapping with high temporal resolution severely limits the number of photons per pixel, we tracked the intracellular temperature distribution by repeating the measurements on the same cells (Supplementary Figure 16). Fluorescence lifetime movies lasting 55 s (heating duration: 500 ms) and 105 s (heating duration: 1 and 5 s), including the duration of IR laser irradiation, were recorded five times in the same cells (Figure 4a,b) and once in 10 different cells (Figure 5a,b and Supplementary Figure 18d), and averaged at the timing when IR laser irradiation was stopped.

Measurement of temperature change during mitochondrial thermogenesis

The mitochondrial stimulus was conducted by quickly adding 1 mL of 200 μM FCCP (Sigma-Aldrich) in fetal bovine serum (FBS)-free culture medium to the studied cells in 1 ml of FBS-free culture medium in a glass base dish. The temperature of the culture medium was maintained at 26.0 °C.

Acknowledgment

We thank Professor Katsunori Hanamura, Professor Takeharu Nagai, Professor Takuro Ideguchi and Dr. Keiichiro Toda for critical comments on this manuscript. We are also grateful for financial support from PRESTO of JST and JSPS KAKENHI (18H03981, 20H05785, 21J14440 and 24H02306).

Author contributions

K.O. organized this work. K.O., M. Takarada, M. Takinoue and T.F. designed this work. M. Takarada and K.O. performed all imaging experiments, and analyzed the data. M. Takarada., M. Takinoue, M.I., and M.M. prepared and performed experiments using liposomes. K.V.T. and H.N. designed and fabricated the microarray chambers. R. S. contributed to the interpretation of the results. K.O. and M.Takarada wrote the paper.

Competing interest statement

The authors declare no competing interests.

Data availability

The data that support the findings of this study are available from the corresponding author upon reasonable request.

Code availability

The programs used for high-speed temperature mapping by reconstructing intracellular fluorescence lifetime (τ_{FAST}) and for the simulations performed in this study are available online:
https://github.com/tkrdmshr/highspeed-tmp-mapping-public-repository.

References

1. Gota, C., Okabe, K., Funatsu, T., Harada, Y. & Uchiyama S. Hydrophilic fluorescent nanogel thermometer for intracellular thermometry. *J. Am. Chem. Soc.* **131**, 2766–2767 (2009).
2. Okabe, K. *et al.* Intracellular temperature mapping with a fluorescent polymeric thermometer and fluorescence lifetime imaging microscopy. *Nat. Commun.* **3**, 705 (2012).
3. Yang, J. M., Yang, H. & Lin, L. Quantum dot nano thermometers reveal heterogeneous local thermogenesis in living cells. *ACS Nano* **5**(6), 5067–5071 (2011).
4. Kriszt, R. *et al.* Optical visualisation of thermogenesis in stimulated single-cell brown adipocytes. *Sci. Rep.* **7**(1), 1–14 (2017).
5. Rajagopal, M. C. *et al.* Transient heat release during induced mitochondrial proton uncoupling. *Commun. Biol.* **2**(1), 1–6 (2019).

6. Fujiwara, M. *et al.* Real-time nanodiamond thermometry probing in vivo thermogenic responses. *Sci. Adv.* **6**(37), eaba9636 (2020).
7. Di X. *et al*., Quantitatively Monitoring In Situ Mitochondrial Thermal Dynamics by Upconversion Nanoparticles, *Nano Lett*., **21**, 1651–1658 (2021).
8. Kiyonaka, S. *et al.* Genetically encoded fluorescent thermosensors visualize subcellular thermoregulation in living cells. *Nat. Methods* **10**(12), 1232–1238 (2013).
9. Nakano, M. *et al.* Genetically encoded ratiometric fluorescent thermometer with wide range and rapid response. *PLoS One* **12**(2), e0172344 (2017).
10. Piñol, R. *et al.* Real-time intracellular temperature imaging using lanthanide-bearing polymeric micelles. *Nano Lett.* **20**(9), 6466–6472 (2020).
11. Di, X., Wang, D., Su, Q.P., Liu, Y., Liao, J., Maddahfar, M., Zhou, J., Jin, D. Spatiotemporally mapping temperature dynamics of lysosomes and mitochondria using cascade organelle-targeting upconversion nanoparticles. *Proc. Natl. Acad. Sci. USA*, **119**, e2207402119 (2022).
12. Zhou, J., Del Rosal, B., Jaque, D., Uchiyama, S. & Jin, D. Advances and challenges for fluorescence nanothermometry. *Nat. Methods* **17**(10), 967–980 (2020).
13. Okabe, K., Sakaguchi, R., Shi, B. & Kiyonaka, S. Intracellular thermometry with fluorescent sensors for thermal biology. *Pflügers Archiv Eur. J. Physiol.* **470**(5), 717–731 (2018).
14. Evanko, D. A thermometer for cells. *Nat. Methods* **9**, 328 (2012).
15. Okabe, K. & Uchiyama S., Intracellular thermometry uncovers spontaneous thermogenesis and associated thermal signaling, *Commun Biol* **4**, 1377 (2021).
16. Baffou, G., Rigneault, H., Marguet, D. & Jullien, L. A critique of methods for temperature imaging in single cells. *Nat. Methods* **11**(9), 899–901 (2014).
17. Maeda, Y. T., Tlusty, T. & Libchaber, A. Effects of long DNA folding and small RNA stem–loop in thermophoresis. *Proc. Natl. Acad. Sci. USA* **109**, 17972–17977 (2012).
18. Becker, W. Fluorescence lifetime imaging–techniques and applications. *J. Microscopy* **247**(2), 119–136 (2012).
19. Kamei, Y. *et al.* Infrared laser-mediated gene induction in targeted single cells in vivo. *Nat. Methods* **6**, 79–81 (2009).
20. Ebbinghaus S., Dhar A., McDonald J. D. & Gruebele M. Protein folding stability and dynamics imaged in a living cell. *Nat. Methods* **7**, 319–323 (2010).
21. Gota, C., Uchiyama, S., Yoshihara, T., Tobita, S. & Ohwada, T. Temperature-dependent fluorescence lifetime of a fluorescent polymeric thermometer, poly(*N*-isopropylacrylamide), labeled by polarity and hydrogen bonding sensitive 4-sulfamoyl-7-aminobenzofurazan. *J. Phys. Chem. B* **112**(10), 2829–2836 (2008).
22. Kubin, R. F. & Fletcher, A. N. Fluorescence quantum yields of some rhodamine dyes. *J. Luminescence* **27**(4), 455–462 (1982).
23. Moreau, D., Lefort, C., Burke, R., Leveque, P. & O'Connor, R. P. Rhodamine B as an optical thermometer in cells focally exposed to infrared laser light or nanosecond pulsed electric fields. *Biomed. Opt. Exp.* **6**(10), 4105–4117 (2015).
24. Toda K., *et al.*, Label-free mid-infrared photothermal microscopy revisits intracellular thermal dynamics: what

do fluorescent nanothermometers measure? *arXiv*:2406.16265.
25. Bothe, J. R., Nikolova, E. N., Eichhorn, C. D., Chugh, J., Hansen, A. L. & Al-Hashimi, H. M. Characterizing RNA dynamics at atomic resolution using solution-state NMR spectroscopy. *Nat. Methods* **8**(11), 919–931 (2011).
26. Boulos, M. I., Fauchais, P., & Pfender, E. *Thermal plasmas* (Vol. 1). 5−8. Springer Science & Business Media. (1994).
27. Novko, D., Caruso, F., Draxl, C., & Cappelluti, E. Ultrafast Hot Phonon Dynamics in MgB 2 Driven by Anisotropic Electron-Phonon Coupling. *Phys. Rev. Lett.* **124**(7), 077001 (2020).
28. Ximendes, E. C. *et al.* Unveiling in vivo subcutaneous thermal dynamics by infrared luminescent nanothermometers. *Nano Lett.* **16**(3), 1695–1703 (2016).
29. Sotoma, S. *et al.* In situ measurements of intracellular thermal conductivity using heater-thermometer hybrid diamond nanosensors. *Sci. Adv.* **7**(3), eabd7888 (2021).
30. Hoshi, Y. *et al.* Ischemic brain injury leads to brain edema via hyperthermia-induced TRPV4 activation. *J. Neurosci.* **38**, 5700–5709 (2018).
31. Chuma, S. *et al.*, Implication of thermal signaling in neuronal differentiation revealed by manipulation and measurement of intracellular temperature. *Nat. Commun.* **15**, 3473 (2024).
32. Shibasaki, K. *et al.* Temperature elevation in epileptogenic foci exacerbates epileptic discharge through TRPV4 activation. *Lab. Invest.* **100**, 274–284 (2020).
33. Yang, X. F., Chang, J. H. & Rothman, S. M. Intracerebral temperature alterations associated with focal seizures. *Epilepsy Res.* **52**(2), 97–105 (2002).
34. Zhu, X., Li, J., Qiu, X., Liu, Y., Feng, W. & Li, F. Upconversion nanocomposite for programming combination cancer therapy by precise control of microscopic temperature. *Nat. Commun.* **9**, 2176 (2018).
35. Evans, S. S., Repasky, E. A. & Fisher, D. T. Fever and the thermal regulation of immunity: the immune system feels the heat. *Nat. Rev. Immunol.* **15**(6), 335–349 (2015).
36. Rodenfels, J., Neugebauer, K. M. & Howard, J. Heat oscillations driven by the embryonic cell cycle reveal the energetic costs of signaling. *Dev. Cell* **48**, 646–658 (2019).
37. Choi, J. *et al.* Probing and manipulating embryogenesis via nanoscale thermometry and temperature control. *Proc. Natl. Acad. Sci. USA* **117**, 14636–14641 (2020).
38. Ermakova, Y. G. *et al.* Thermogenetic neurostimulation with single-cell resolution. *Nat. Commun.* **8**, 15362 (2017).
39. Falahati, H. & Wieschaus, E. Independent active and thermodynamic processes govern the nucleolus assembly *in vivo*. *Proc. Natl. Acad. Sci. USA* **114**, 1335–1340 (2017).
40. Soumpasis, D. M. Theoretical analysis of fluorescence photobleaching recovery experiments. *Biophys. J.* **41**, 95–97 (1983).
41. Watanabe, R. *et al.* Arrayed lipid bilayer chambers allow single-molecule analysis of membrane transporter activity. *Nat. Commun.* **5**, 4519 (2014).

Figure legends

Figure 1. High-resolution mapping of temperature in living COS7 cell with τ_{FAST}-based FLIM.

a. Functional diagram of FPT responding above the lower critical solution temperature (LCST) and its temperature response curve using conventional fluorescence lifetime (τ_f).

b. Schematic diagram of fluorescence lifetime determination in FLIM. In the conventional analysis, the fluorescence lifetime (τ_f) is calculated from the parameters obtained by approximating the fluorescence decay curve with a two-component exponential function, while the fast fluorescence lifetime (τ_{FAST}) is obtained by just averaging the arrival time (τ_{arr}) of photons in TCSPC. A and N represent amplitude and number of photons, respectively.

c. The temperature response curve (closed, left axis) and temperature resolution (open, right axis) of FPT using fast fluorescence lifetime (τ_{FAST}).

d. The relationship between the standard deviation of fluorescence lifetime (τ_f: black and τ_{FAST}: red) and photon counts in TCSPC-FLIM.

e. Comparison of fluorescence lifetime images of FPT using τ_{FAST} with various accumulation times.

f. Fluorescence lifetime (τ_{FAST}) images of FPT. The region of interest, as shown in the square in the left panel, is enlarged in the right panel.

g. Comparison of temperature distribution in aqueous solution and in the cytoplasm of a cell.

h. The colocalization of the intracellular area with a higher temperature than the surroundings (middle) with mitochondria visualized using MitoTracker Deep Red FM (left). Histogram of fluorescence lifetime (τ_{FAST}) is shown on the right. Dotted line indicates the outline of the cell. ΔT was calculated by subtracting the average temperature around mitochondria from that of cytoplasm. $<\Delta T>$ represents an average of the histogram.

Scale bars represent 10 μm.

Figure 2. Local heating using IR laser in living COS7 cell.

a. Optical set-up.

b. Fluorescence lifetime images of FPT without (Off) and with (On) IR laser irradiation (0.55 mW). The right graph indicates the profile of ΔT of the cell. ΔT was calculated by subtracting the temperature distribution during heating from that of before heating.

c. The relationship between IR laser power and the increase in averaged temperature of whole cells (ΔT_{ave}). Data are presented as mean ± s.e.m. ($n \geq 29$ cells).

d. Reversibility of the fluorescence lifetime response of FPT to local heating (IR laser: 0.67 mW). The right graph shows the fluorescence lifetime of a 10 μm diameter area indicated by a line in the left image.

Figure 3. Monitoring temperature variation upon heating with IR laser in living COS7 cell and liposome.

a. Tracking of the average temperature of a whole cell when heated by continuous (red, 0.55 mW for 5 s) and pulsed (black, 1.1 mW for 0.1 s) irradiation with an IR laser (left). Normalized temperature relaxation of these two alternatives was compared (right). Data including the inset in the right graph are mean ± s.e.m. [n = 29 (continuous), 15 (pulsed) cells].

b. Tracking of the average temperature of a square area with a 10 μm side centered on the heating point upon heating by continuous (red, 0.55 mW for 5 s) and pulsed (black, 1.1 mW for 0.1 s) irradiation of an IR laser (left). Normalized temperature relaxation of these two alternatives was compared (right). Data including the inset in the right graph are

mean ± s.e.m. [n = 30 (continuous), 15 (pulsed) cells].

c. The tracking of average temperature of a square area with a 10 μm side centered on the heating point in the nucleus (red) was compared with that in the cytoplasm (**b**, black) of cells upon continuous heating (0.55 mW for 5 s) (left). Normalized temperature relaxation of these two regions was compared (right). Data including the inset in the right graph are mean ± s.e.m. (n = 30 cells).

d. Comparison of average temperature changes of intracellular square area with a 10 μm side centered on the heating point (red) and that of water in liposomes (black) upon continuous heating (0.83 mW for 5 s) (left). Normalized temperature relaxation of these two regions was compared (right). Data including the inset in the right graph are mean ± s.e.m. [n = 10 (liposome), 30 (cell)].

Insets in the right panels of **a**,**b**,**c**,**d** indicate areas under the curves (AUC) of normalized temperature relaxation. $^{***}P < 0.001$ (Welch's t test). Vertical scale bars in the right panels of **a**,**b**,**c**,**d** represent indicated temperature changes. ΔT was calculated by subtracting the average temperature from that of before heating.

Figure 4. Independence of intracellular temperature relaxation after continuous heating on the heat conduction model.

a. The temperature mapping of a whole cell with local heating (0.83 mW for 1 s). The tracking of average temperature (left) and representative temperature distributions in cells at various time points. The cell is indicated by a dotted line (right). Scale bar represents 10 μm.

b. The intracellular temperature distribution with different heating conditions [top (0.55 mW for 5 s), middle (0.83 mW for 1 s), and bottom (0.89 mW for 500 ms)]. The line profiles of ΔT of cells and the temperature mapping during relaxation are also shown. Scale bars represent 10 μm.

c. The tracking of average temperature of the whole cell, normalized temperature relaxation, and its area under the curve (AUC, inset). Data in the inset are mean ± s.e.m. (n = 10 cells). Vertical scale bars represent temperature change.

d. The average temperature relaxation for various spatial sizes was analyzed from the time course of the temperature distribution numerically calculated by the heat conduction equation in Supplementary Note 4. Areas of diameter (D) = 3, 5, and 10 μm are shown.

e. The relaxation of average temperature of various sized regions observed in the cytoplasm of living COS7 cells after continuous heating (5 s) (Figure 3**b**). Data in cells are presented as mean ± s.e.m. (n = 30 cells). Areas of a square with a side (L) = 3, 5, and 10 μm are shown.

f. Comparison of the size dependence of temperature relaxation times between the simulation based on the heat conduction equation and the observation in living COS7 cells. The relationship between the region size and the temperature relaxation rates evaluated using fold change in area under the curve (AUC).

a-c. ΔT was calculated by subtracting the temperature from that of after the temperature relaxation.

Figure 5. Observation of slow temperature relaxation in intracellular local area by high-speed intracellular temperature mapping.

High-speed mapping of intracellular temperature in the cytoplasm (**a**) and in the nucleus (**b**) immediately after stopping local heating [1.1 mW (cytoplasm) and 0.83 mW (nucleus) for 5 s]. Fluorescence lifetime images were taken every 41 ms. The right graphs show the relaxation of average temperature in the heating areas indicated in the left

images. ΔT was calculated by subtracting the temperature from that of after the temperature relaxation. Scale bars represent 2 μm.

Figure 1

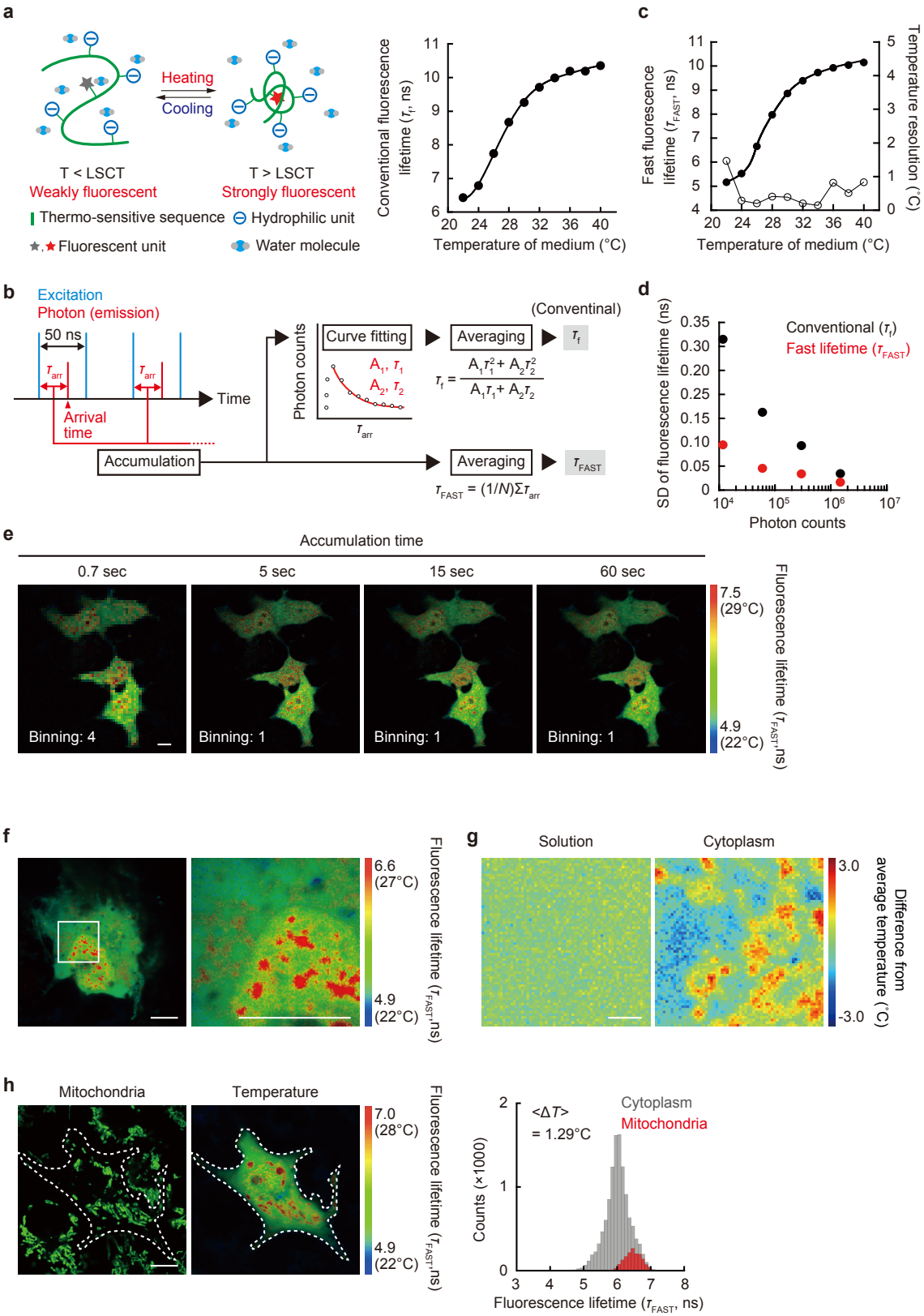
a
Heating
Cooling
T < LSCT
Weakly fluorescent
T > LSCT
Strongly fluorescent
Thermo-sensitive sequence
Hydrophilic unit
Fluorescent unit
Water molecule
Conventional fluorescence lifetime (τ_f, ns)
Temperature of medium (°C)
c
Fast fluorescence lifetime (τ_{FAST}, ns)
Temperature resolution (°C)
Temperature of medium (°C)
b
Excitation
Photon (emission)
50 ns
τ_{arr}
Arrival time
Time
Accumulation
Photon counts
Curve fitting
A_1, τ_1
A_2, τ_2
τ_{arr}
(Conventional)
Averaging
τ_f
$\tau_f = \frac{A_1\tau_1^2 + A_2\tau_2^2}{A_1\tau_1 + A_2\tau_2}$
Averaging
τ_{FAST}
$\tau_{FAST} = (1/N)\Sigma\tau_{arr}$
d
SD of fluorescence lifetime (ns)
Conventional (τ_f)
Fast lifetime (τ_{FAST})
Photon counts
e
Accumulation time
0.7 sec
5 sec
15 sec
60 sec
Binning: 4
Binning: 1
Binning: 1
Binning: 1
7.5 (29°C)
4.9 (22°C)
Fluorescence lifetime (τ_{FAST}, ns)
f
6.6 (27°C)
4.9 (22°C)
Fluorescence lifetime (τ_{FAST}, ns)
g
Solution
Cytoplasm
3.0
-3.0
Difference from average temperature (°C)
h
Mitochondria
Temperature
7.0 (28°C)
4.9 (22°C)
Fluorescence lifetime (τ_{FAST}, ns)
<ΔT> = 1.29°C
Cytoplasm
Mitochondria
Counts (×1000)
Fluorescence lifetime (τ_{FAST}, ns)

Figure 1. High-resolution mapping of temperature in living COS7 cell with τ_{FAST}-based FLIM.
a. Functional diagram of FPT responding above the lower critical solution temperature (LCST) and its temperature response curve using conventional fluorescence lifetime (τ_f). **b.** Schematic diagram of fluorescence lifetime determination in FLIM. In the conventional analysis, the fluorescence lifetime (τ_f) is calculated from the parameters obtained by approximating the fluorescence decay curve with a two-component exponential function, while the fast fluorescence lifetime (τ_{FAST}) is obtained by just averaging the arrival time (τ_{arr}) of photons in TCSPC. A and N represent amplitude and number of photons, respectively. **c.** The temperature response curve (closed, left axis) and temperature resolution (open, right axis) of FPT using fast fluorescence lifetime (τ_{FAST}). **d.** The relationship between the standard deviation of fluorescence lifetime (τ_f: black and τ_{FAST}: red) and photon counts in TCSPC-FLIM. **e.** Comparison of fluorescence lifetime images of FPT using τ_{FAST} with various accumulation times. **f.** Fluorescence lifetime (τ_{FAST}) images of FPT. The region of interest, as shown in the square in the left panel, is enlarged in the right panel. **g.** Comparison of temperature distribution in aqueous solution and in the cytoplasm of a cell. **h.** The colocalization of the intracellular area with a higher temperature than the surroundings (middle) with mitochondria visualized using MitoTracker Deep Red FM (left). Histogram of fluorescence lifetime (τ_{FAST}) is shown on the right. Dotted line indicates the outline of the cell. ΔT was calculated by subtracting the average temperature around mitochondria from that of cytoplasm. $<\Delta T>$ represents an average of the histogram. Scale bars represent 10 μm.

Figure 2

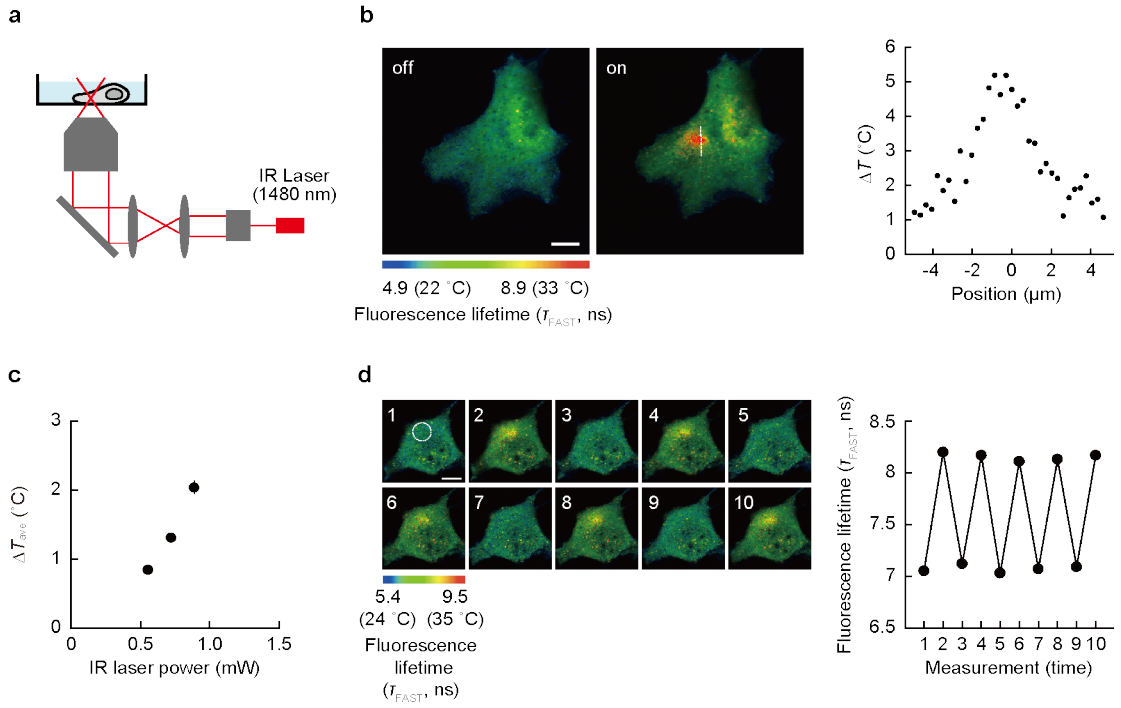

Figure 2. Local heating using IR laser in living COS7 cell.

a. Optical set-up. **b.** Fluorescence lifetime images of FPT without (Off) and with (On) IR laser irradiation (0.55 mW). The right graph indicates the profile of ΔT of the cell. ΔT was calculated by subtracting the temperature distribution during heating from that of before heating. **c.** The relationship between IR laser power and the increase in averaged temperature of whole cells (ΔT). Data are presented as mean ± s.e.m. ($n \geq 29$ cells). **d.** Reversibility of the fluorescence lifetime response of FPT to local heating (IR laser: 0.67 mW). The right graph shows the fluorescence lifetime of a 10 μm diameter area indicated by a line in the left image.

Figure 3

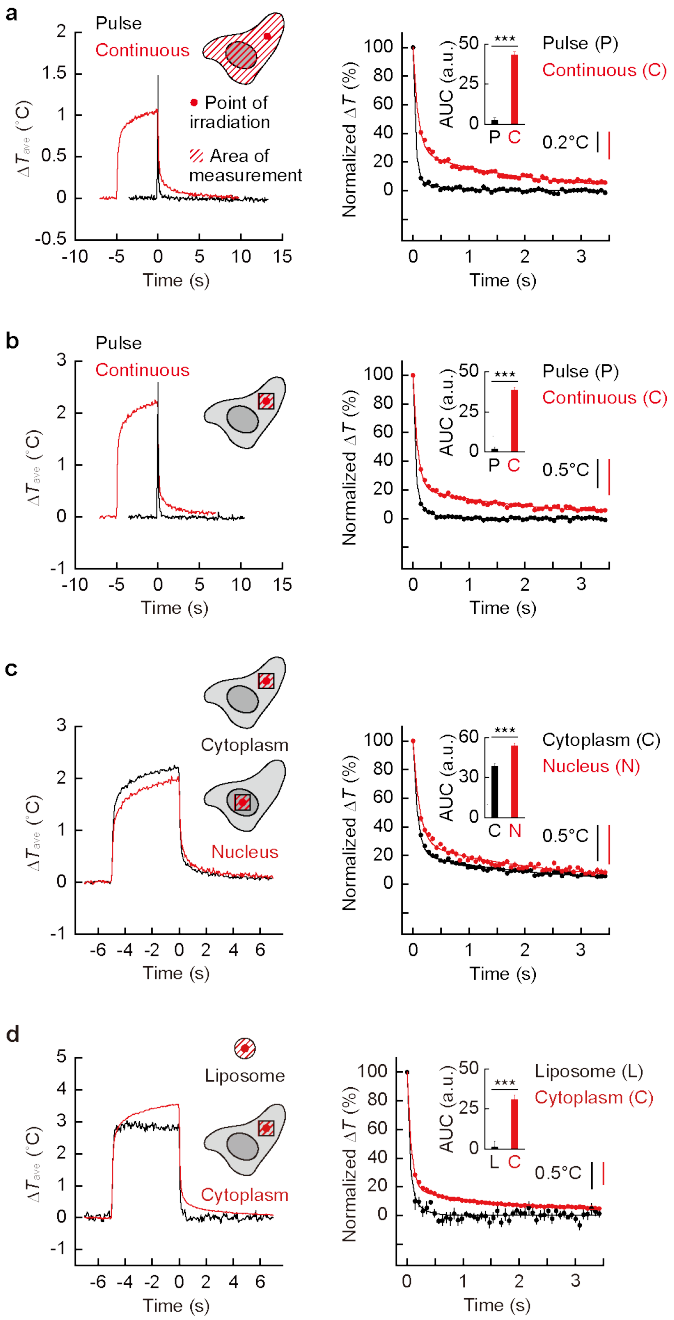
a
Pulse
Continuous
Point of irradiation
Area of measurement
ΔTave (°C)
Time (s)
Normalized ΔT (%)
AUC (a.u.)
***
P C
Pulse (P)
Continuous (C)
0.2°C
b
Pulse
Continuous
0.5°C
c
Cytoplasm
Nucleus
C N
Cytoplasm (C)
Nucleus (N)
d
Liposome
L C
Liposome (L)
Cytoplasm (C)

Figure 3. Monitoring temperature variation upon heating with IR laser in living COS7 cell and liposome. **a.** Tracking of the average temperature of a whole cell when heated by continuous (red, 0.55 mW for 5 s) and pulsed (black, 1.1 mW for 0.1 s) irradiation with an IR laser (left). Normalized temperature relaxation of these two alternatives was compared (right). Data including the inset in the right graph are mean ± s.e.m. [n = 29 (continuous), 15 (pulsed) cells]. **b.** Tracking of the average temperature of a square area with a 10 μm side centered on the heating point upon heating by continuous (red, 0.55 mW for 5 s) and pulsed (black, 1.1 mW for 0.1 s) irradiation of an IR laser (left). Normalized temperature relaxation of these two alternatives was compared (right). Data including the inset in the right graph are mean ± s.e.m. [n = 30 (continuous), 15 (pulsed) cells]. **c.** The tracking of average temperature of a square area with a 10 μm side centered on the heating point in the nucleus (red) was compared with that in the cytoplasm (**b**, black) of cells upon continuous heating (0.55 mW for 5 s) (left). Normalized temperature relaxation of these two regions was compared (right). Data including the inset in the right graph are mean ± s.e.m. (n = 30 cells). **d.** Comparison of average temperature changes of intracellular square area with a 10 μm side centered on the heating point (red) and that of water in liposomes (black) upon continuous heating (0.83 mW for 5 s) (left). Normalized temperature relaxation of these two regions was compared (right). Data including the inset in the right graph are mean ± s.e.m. [n = 10 (liposome), 30 (cell)]. Insets in the right panels of **a,b,c,d** indicate areas under the curves (AUC) of normalized temperature relaxation. ***$P < 0.001$ (Welch's t test). Vertical scale bars in the right panels of **a,b,c,d** represent indicated temperature changes. ΔT was calculated by subtracting the average temperature from that of before heating.

Figure 4

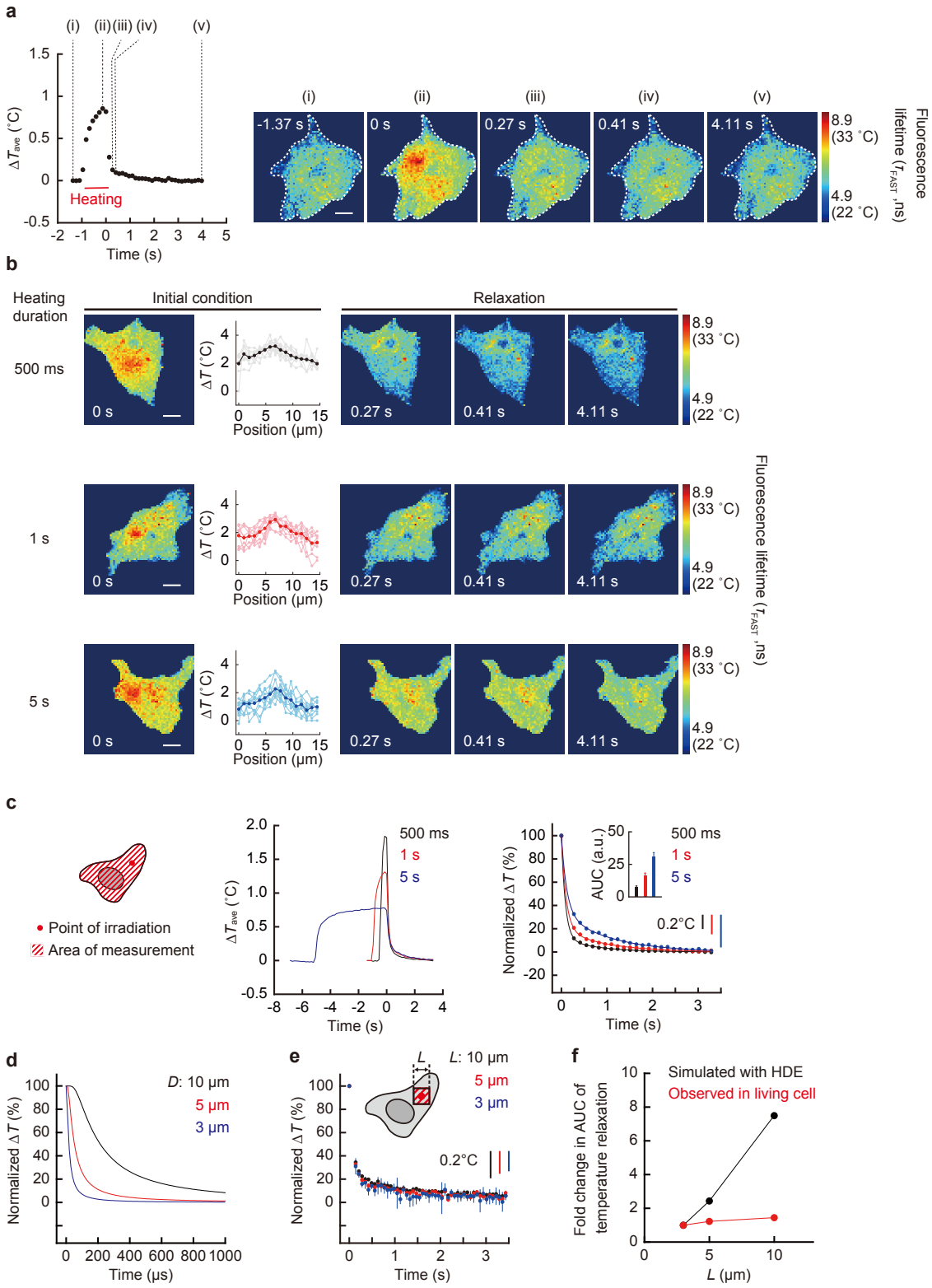
a
(i) (ii) (iii) (iv) (v)
ΔTave (°C)
Heating
Time (s)
-1.37 s
0 s
0.27 s
0.41 s
4.11 s
8.9 (33 °C)
4.9 (22 °C)
Fluorescence lifetime (τFAST, ns)
b
Heating duration
Initial condition
Relaxation
500 ms
1 s
5 s
ΔT (°C)
Position (μm)
c
Point of irradiation
Area of measurement
500 ms
1 s
5 s
Normalized ΔT (%)
AUC (a.u.)
0.2°C
d
D: 10 μm
5 μm
3 μm
Time (μs)
e
L
L: 10 μm
f
Simulated with HDE
Observed in living cell
Fold change in AUC of temperature relaxation
L (μm)

Figure 4. Independence of intracellular temperature relaxation after continuous heating on the heat conduction model.

a. The temperature mapping of a whole cell with local heating (0.83 mW for 1 s). The tracking of average temperature (left) and representative temperature distributions in cells at various time points. The cell is indicated by a dotted line (right). Scale bar represents 10 μm. **b.** The intracellular temperature distribution with different heating conditions [top (0.55 mW for 5 s), middle (0.83 mW for 1 s), and bottom (0.89 mW for 500 ms)]. The line profiles of ΔT of cells and the temperature mapping during relaxation are also shown. Scale bars represent 10 μm. **c.** The tracking of average temperature of the whole cell, normalized temperature relaxation, and its area under the curve (AUC, inset). Data in the inset are mean ± s.e.m. (n = 10 cells). Vertical scale bars represent temperature change. **d.** The average temperature relaxation for various spatial sizes was analyzed from the time course of the temperature distribution numerically calculated by the heat conduction equation in Supplementary Note 4. Areas of diameter (D) = 3, 5, and 10 μm are shown. **e**. The temperature relaxation of average temperature of various sized regions observed in the cytoplasm of living COS7 cells after continuous heating (5 s) (Figure 3**b**) (middle). Data in cells are presented as mean ± s.e.m. (n = 30 cells). Areas of a square with a side (L) = 3, 5, and 10 μm are shown. **f**. Comparison of the size dependence of temperature relaxation times between the simulation based on the heat conduction equation and the observation in living COS7 cells. The relationship between the region size and the temperature relaxation rates evaluated using fold change in area under the curve (AUC) (right). **a-c.** ΔT was calculated by subtracting the temperature from that of after the temperature relaxation.

Figure 5

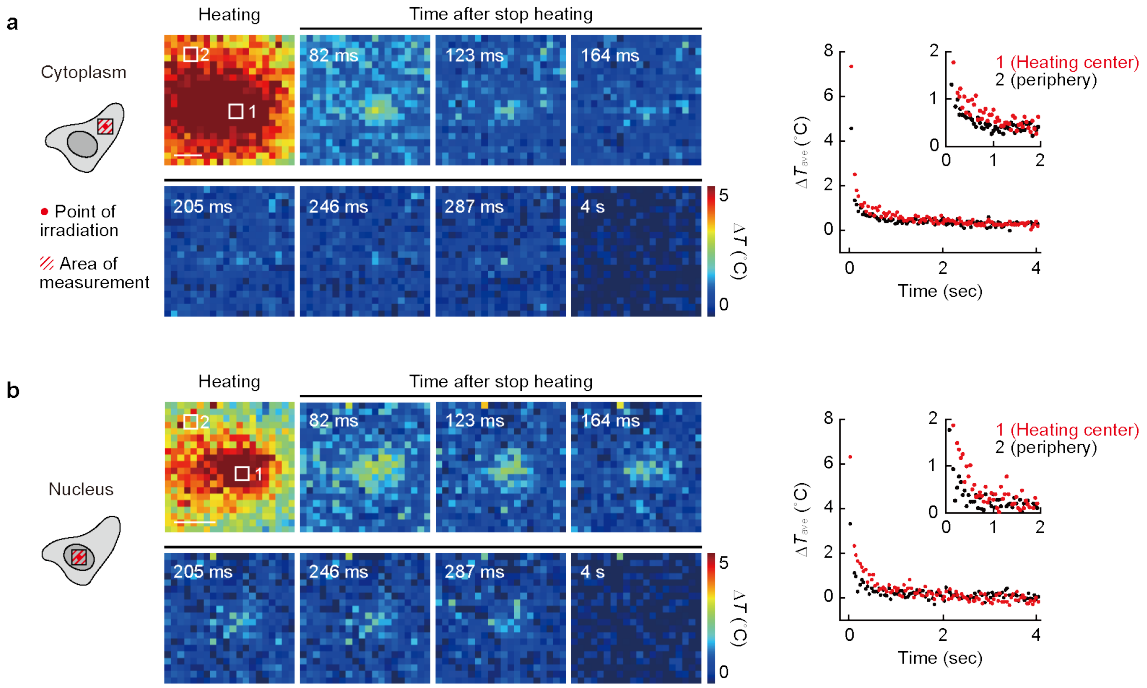

Figure 5. Observation of slow temperature relaxation in intracellular local area by high-speed intracellular temperature mapping.

High-speed mapping of intracellular temperature in the cytoplasm (**a**) and in the nucleus (**b**) immediately after stopping local heating [1.1 mW (cytoplasm) and 0.83 mW (nucleus) for 5 s]. Fluorescence lifetime images were taken every 41 ms. The right graphs show the relaxation of average temperature in the heating areas indicated in the left images. ΔT was calculated by subtracting the temperature from that of after the temperature relaxation. Scale bars represent 2 μm.

Supplementary information for:

High-speed Intracellular Temperature Mapping Reveals the Existence of Non-Conductive Dissipation of Energy by Heating

Masaharu Takarada, Ryo Shirakashi, Masahiro Takinoue, Motohiko Ishida, Masamune Morita, Hiroyuki Noji, Kazuhito V. Tabata, Takashi Funatsu and Kohki Okabe

Supplementary Notes

Supplementary Note 1. Fast fluorescence lifetime (τ_{FAST}) of FPT for determination of temperature change in cell

In the TCSPC used in this method, the fluorescence emission time after excitation, which is obtained by measuring the arrival time of photons of FPT detected synchronously with the excitation pulse laser (20 MHz), is integrated by repeated scanning (Figure 1b). In the conventional analysis of fluorescence lifetime, the average fluorescence lifetime (τ_f) is obtained from the value of each component obtained by approximating the fluorescence decay curve drawn using a large number of photons integrated over a long time (60 s) with a two-component exponential function. In contrast, the fast lifetime (τ_{FAST}) is simply determined from averaging the average arrival time of the obtained photons (Figure 1b).

The τ_f of FPT is slightly longer than the τ_{FAST} because elimination of the excitation pulse-derived signal (instrumental response function, IRF) was performed by limiting the approximation range (fluorescence decay curves below 2.5 ns were excluded) when calculating the conventional fluorescence lifetime.

In determining the intracellular temperature change (ΔT) during heating by an artificial heat source, we used the temperature response curve of τ_{FAST} of FPT (Figure 1c) as a calibration when the entire cell was heated to ignore the temperature increase due to steady-state spontaneous heat generation of cells. For intracellular temperature mapping, we used a previously established calibration method using cell extracts[2] (Supplementary Figure S1).

Supplementary Note 2. Confirmation of temporal and spatial resolution of intracellular temperature measurement by the fast fluorescence lifetime (τ_{FAST}) of FPT

In high-speed temperature tracking, the response time of FPT can affect its spatio-temporal resolution. Because the time required for the conformational change of FPT has been unknown, we investigated this by using a controllable artificial heat source. Polyacrylamide polymer, the main backbone of FPT, exhibits a temperature-dependent phase transition above the lower critical solution temperature (LCST), causing FPT to respond within a specific temperature range (Supplementary Figure S6a). During the process of temperature relaxation to below the LCST of FPT after the heating stops, the fluorescence lifetime change of FPT is determined almost entirely by its structural relaxation, not by the temperature relaxation (Supplementary Figure S6a). In the temperature tracking experiments of this study, the

base temperature and the temperature during heating were set within the range where the FPT is temperature-responsive (Supplementary Figure S6a). Here, cells cultured at a low temperature (13°C), at which FPT is not temperature-responsive, were heated by an IR laser to a temperature (31°C) at which FPT is temperature-responsive. Supplementary Figure S6b shows the rapid relaxation of the fast lifetime of FPT in cells measured with high temporal resolution (every 9 ms) after the heating was stopped. Given that the first frame after the fluorescence lifetime drop does not reflect the temperature, the result indicates that the time of structural relaxation of FPT obtained both in solution and in cells are equal to or less than the time of scanning (9 ms). This value was used to discuss the temporal (**a**) and the spatial (**b**) resolution of temperature measurement using FPT.

(a) Temporal resolution

The parameters related to the temporal resolution include the fluorescence lifetime of FPT (~10 ns); the scanning time for fluorescence lifetime imaging (9 ms); the time required for photon integration, which is calculated as 1.4 ms based on the number of photons required to determine the fluorescence lifetime with an accuracy of 0.1 ns (Fig. 1d) and a photon acquisition efficiency of 8.2×10^3 ms^{-1}; and the response time of FPT (< 9 ms). Among these factors, the scanning time for fluorescence lifetime imaging (9 ms) is the rate-limiting step, which determines the temporal resolution of this intracellular temperature measurement.

(b) Spatial resolution

The error (e.g., spatial resolution) with respect to spatial information in temperature mapping using FPT is determined by the diffraction limit of light in microscopy or the distance traveled within the response time of diffusing FPT (as described above, less than 9 ms: Supplementary Figure S6). The molecular diffusion time of FPT in cells was quantified by the fluorescence recovery after photobleaching (FRAP) method (D_{FPT} = 0.13 $\mu m^2 s^{-1}$: Supplementary Figure S7). The distance that FPT moves by diffusion within the time required for the structural transition of FPT upon temperature change was calculated from the following equation:

$$\Delta x^2 = 4Dt \qquad \text{(S1)}$$

where x is the displacement distance, D is the diffusion constant, and t is the time. Because this calculated distance (below 0.07 μm) is smaller than the diffraction limit of light (0.28 μm), the spatial resolution is determined by the diffraction limit of light.

Supplementary Note 3. Analysis of time constants for intracellular temperature relaxation

The time course of the intracellular temperature after 70 msec after continuous heating in Figure 3a was approximated by the following equation:

$$\Delta T(t) = \sum_{i=1}^{N} \left[A_i exp\left(-\frac{t}{\tau_i}\right) + C_i \right] \qquad \text{(S2)}$$

where A_i, τ_i and C_i represent amplitude, time constant and ΔT after infinite time of components i respectively. Calculations with increasing values of N until the t-test value >2 was no longer satisfied detected a maximum of two components of relaxations: the measured 231 ± 1.53 msec (47.6%) and 3.33 ± 0.141 sec (17.9%), and relaxation earlier than the tracking limit accounted for 34.5% (ΔT after infinite time was 0).

Supplementary Note 4. Estimation of the temperature relaxation time in living cell based on heat conduction

The temperature relaxation time observed in cells was compared to that calculated with the assumption of heat conduction. The temperature change due to heat conduction after the supply of heat is stopped follows the heat conduction equation:

$$\frac{\partial(r\Delta T)}{\partial t} = \kappa \frac{\partial^2(r\Delta T)}{\partial t^2}; \qquad \text{(S3)}$$

$$\Delta T|_{t=0} = \begin{Bmatrix} \Delta T_0; 0 < r < a \\ 0; a < r \end{Bmatrix}$$

where ΔT is temperature, c is specific heat, ρ is density and λ is thermal conductivity. $\kappa=\lambda/\rho c$ is thermal diffusivity. When the temperature in the region of radius a is initially increased by T_0 K relative to the surroundings, the temperature relaxation after the disappearance of the heat source is given by the following exact solution:

$$\Delta T = \frac{\Delta T_0}{2r\sqrt{\pi\kappa t}}\left\{\int_0^a \lambda e^{-\frac{(r-\lambda)^2}{4\kappa t}} d\lambda - \int_0^a \lambda e^{-\frac{(r+\lambda)^2}{4\kappa t}} d\lambda\right\} \qquad \text{(S4)}.$$

Transforming equation (S4), we obtain

$$4\pi r^2 \Delta T = 2\pi r^2 \Delta T_0 \mathrm{Erf}\left[\frac{r-a}{\sqrt{4\kappa t}}, \frac{r+a}{\sqrt{4\kappa t}}\right] - 4r\Delta T_0\sqrt{\pi\kappa t}\left\{e^{-\frac{(r-a)^2}{4\kappa t}} - e^{-\frac{(r+a)^2}{4\kappa t}}\right\} \qquad \text{(S5)}.$$

Note) $\mathrm{Erf}\,[x, y] \equiv \frac{2}{\sqrt{\pi}}\int_x^y e^{-\eta^2} d\eta$.

From equation (S5), the average temperature in region i ($\Delta T_{av,i}$) is defined as

$$\Delta T_{av,i}(t) \equiv \frac{\int_0^{r_i} 4\pi r^2 T dr}{\frac{4}{3}\pi r_i^3} \qquad \text{(S6)}.$$

The normalized average temperature of region i ($\Delta T_{normal,i}$) is:

$$\Delta T_{normal,i}(t) \equiv \Delta T_{av,i}(t)/\Delta T_{av,i}(0) \qquad \text{(S7)}.$$

Using this equation (S7) and the values of thermal conductivity (λ: 0.1 $Wm^{-1}K^{-1}$)[24,29,41,42], specific heat capacity (c: 3.9 $Jg^{-1}K^{-1}$)[43] and density (ρ: 1.05 gmL^{-1})[44] reported in cells, and the radius of heat source (a: 0.65 μm), we numerically calculated the time course of temperature at an interval of 2 μs. As shown in Supplementary Figure S15, the relaxation time was on the order of ms.

Supplementary Note 5. The nature of the temperature change caused only by heat conduction

To understand the principle of intracellular temperature change, we examined the following two properties of heat conduction.

(a) Independence of the relaxation time of the average temperature on heating duration

The relaxation of temperature distribution in systems following equation (S3), with constant thermal diffusivity without a heat source term, only depends on the distribution of initial temperature. Therefore, when the regions defined for calculating averaged temperature (S6,7) are the same, the relaxation time of the average temperature (ΔT_{av}) is identical and is not dependent on the heating duration. Note that according to the definition (S6), averaged temperature is equivalent to the amount of heat in the given averaged region; once the heat amount of the region is determined, the duration required for heating is irrelevant.

(b) Dependence of the relaxation time of the average temperature on area size

Next, we investigated the temperature change based on the nature of heat transfer by diffusion. In an aqueous solution, heat is dissipated to the surroundings by diffusion. To investigate the temperature change in water caused by heat transfer, we used the heat conduction equation (S3) and performed a numerical simulation of the temperature relaxation after stopping heating. Comparing the average temperature relaxation in regions of different sizes, we found that the time required for relaxation increases with the size of the observed region (Figure 4d).

Supplementary Note 6. Estimation of intracellular temperature increase due to mitochondrial heat generation

Assuming that the dissipation of generated heat is entirely limited by the dominant energy conversion, we calculated the temperature increase due to spontaneous cellular heat generation using the measured intracellular heat dissipation time (approximately 1 s). Carbonyl cyanide 4-(trifluoromethoxy) phenylhydrazone (FCCP), an uncoupling agent in mitochondria, the most common target for measurement in intracellular thermometry, induces heat generation that lasts around 4.2 nW per cell[45]. When this heat remains in a adiabatic cell for 1 s, then the average temperature rise of whole cell can be estimated as follows:

$$\Delta T = \frac{Q}{c\rho V} = \frac{4.2 \times 10^{-9}}{3.9 \times 1.05 \times (0.9 \times 10^{-9})} = 1.1\ K \qquad \text{(S8)}$$

where Q (= 4.2 nW × 1 s) is the amount of heat that remains in the cell, c (= 3.9 $Jg^{-1}K^{-1}$) is the specific heat, ρ (= 1.05 gmL^{-1}) is the density, and V (= 30 μm × 30 μm × 1μm = 0.9 × 10^{-9} mL) is the volume of the cell. Note that this estimation assumes that this heat is shared by all of the cell volume based on the fact that the same dissipation rate and temperature change is recorded regardless of the chemistry of the thermometers, whereas the temperature change would be even larger if heat is shared by only some molecules.

Supplementary Figures

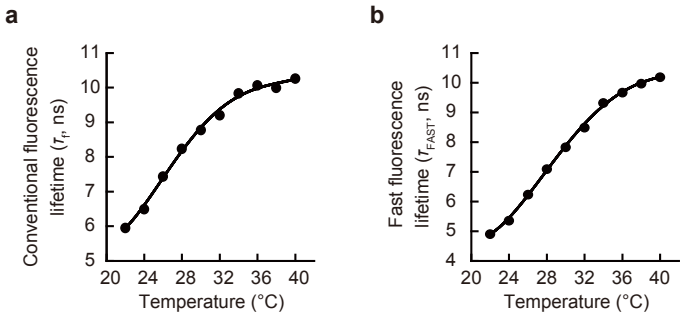

Supplementary Figure S1 | Calibration curve of FPT for intracellular temperature mapping. The temperature-dependent conventional fluorescence lifetime (τ_f, **a**) and fast fluorescence lifetime (τ_{FAST}, **b**) of FPT in a COS7 cell extract.

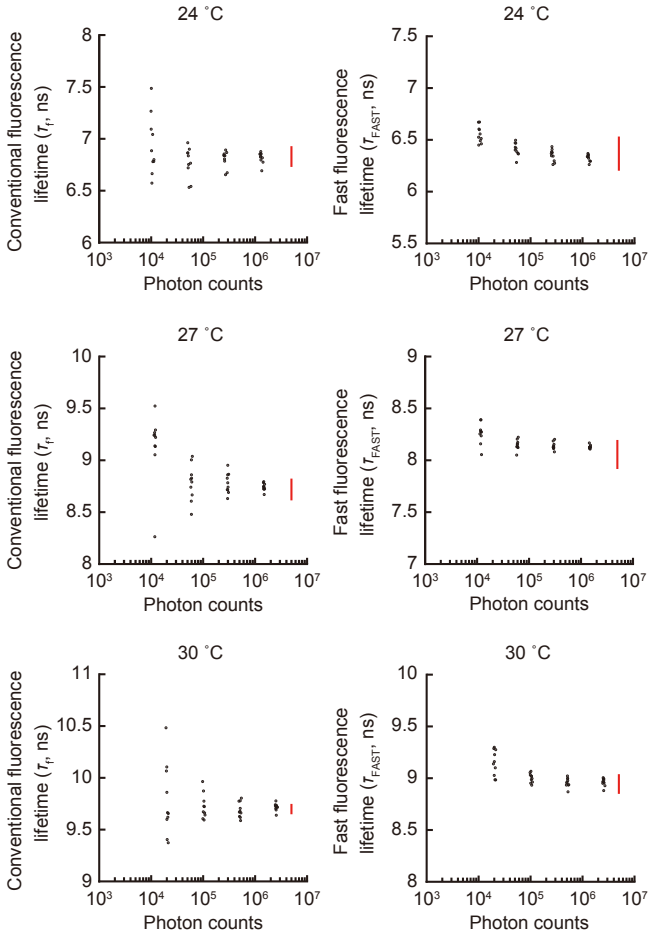

Supplementary Figure S2 | Comparison of photon count-dependent fluorescence lifetime (τ_f vs. τ_{FAST}) variation. The fluorescence lifetime images of FPT were repeatedly obtained ten times and the averaged fluorescence lifetime (τ_f and τ_{FAST}) of a single living COS7 cell was calculated with various accumulating durations corresponding to acquired photon counts. Two kinds of fluorescence lifetime (τ_f and τ_{FAST}) at three temperatures are shown. Red bars indicate the fluorescence lifetime corresponding to 0.5 °C accuracy.

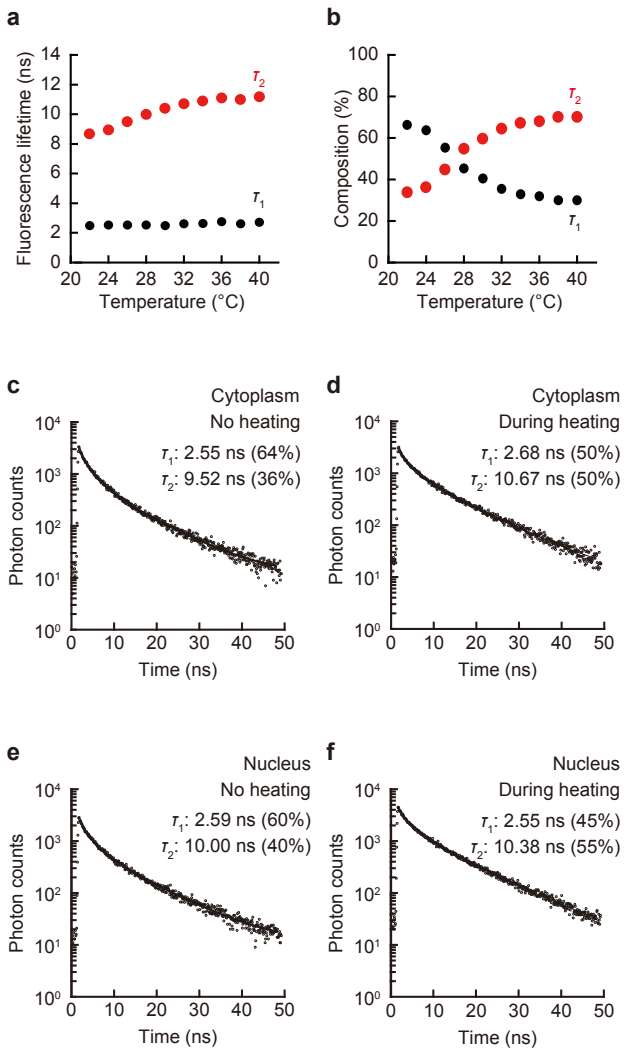

Supplementary Figure S3 | Validation of the temperature increase in the area of IR laser heating based on the change in components (lifetime and composition) of fluorescence lifetime decay of FPT in living COS7 cells. **a**,**b** The medium temperature-dependent two components of fluorescence lifetime decay of FPT in living COS7 cells. Note that these parameters are the values calculated in the analysis of conventional fluorescence lifetime. **a** Fluorescence lifetime–temperature diagram (τ_1, shorter lifetime; τ_2, longer lifetime). **b** Composition–temperature diagram of two components (τ_1 and τ_2). **c-f** Analysis of fluorescence lifetimes (τ_1 and τ_2) and their compositions of fluorescence decay curves of FPT without (**c**,**e**) and with IR laser heating (0.55 mW; **d**,**f**) in the cytoplasm (**c**,**d**) and in the nucleus (**e**,**f**). The changes in two components of fluorescence lifetime and composition were consistent with those of bulk temperature-dependent change in (**a**) and (**b**), confirming that there were no undesired chemical factors involved in the response of FPT.

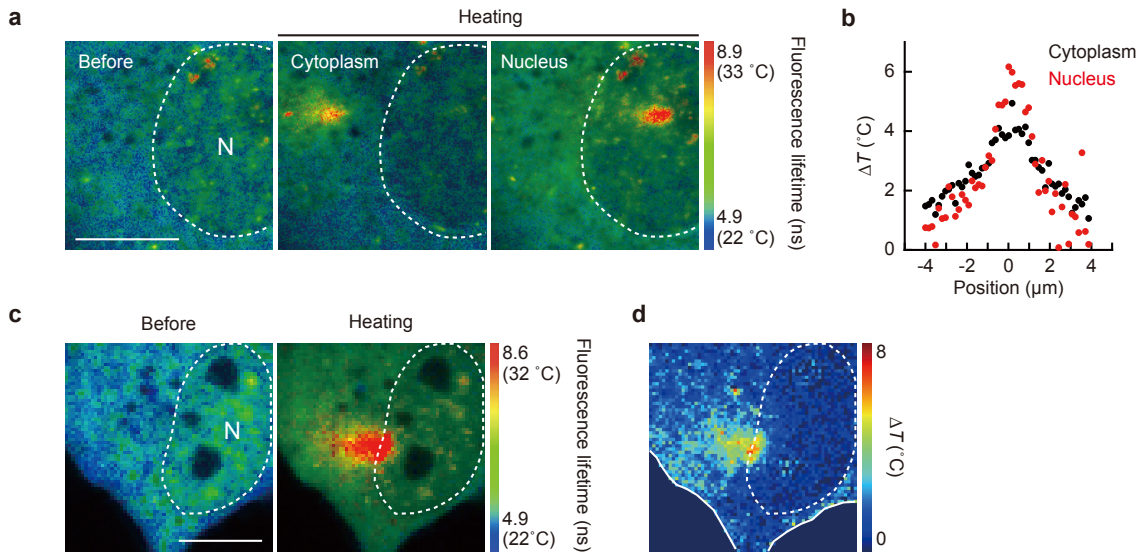

Supplementary Figure S4 | IR laser heating of local regions in living COS7 cells. **a** The steady-state temperature distribution during local heating (IR laser: 0.55 mW) in the cytoplasm and in the nucleus. **b** Line profiles of ΔT of the cytoplasm and the nucleus. **c** The steady-state temperature distribution during local heating on the nuclear membrane. **d** The distribution of temperature increment upon heating (IR laser: 0.55 mW). Scale bars represent 10 μm.

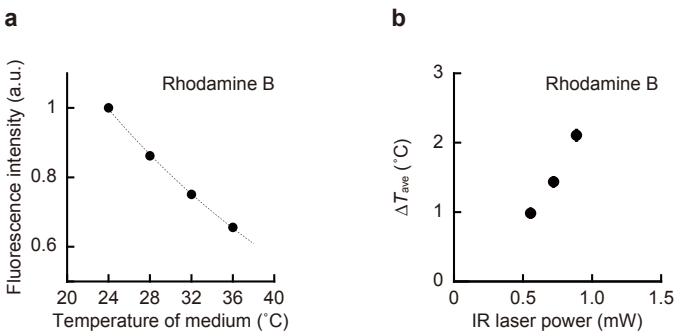

Supplementary Figure S5 | Intracellular thermometry with Rhodamine B in living COS7 cells. a The temperature-dependent fluorescence intensity decrease. An exponential approximation (Fluorescence intensity = $2.3153e^{-0.0351T}$, where T indicates the temperature; $R^2 = 0.99$) was used for the estimation of intracellular temperature change (ΔT). **b** The relationship between IR laser power and the temperature increase of whole cells (ΔT). Data are presented as mean ± s.e.m. (n = 20 cells).

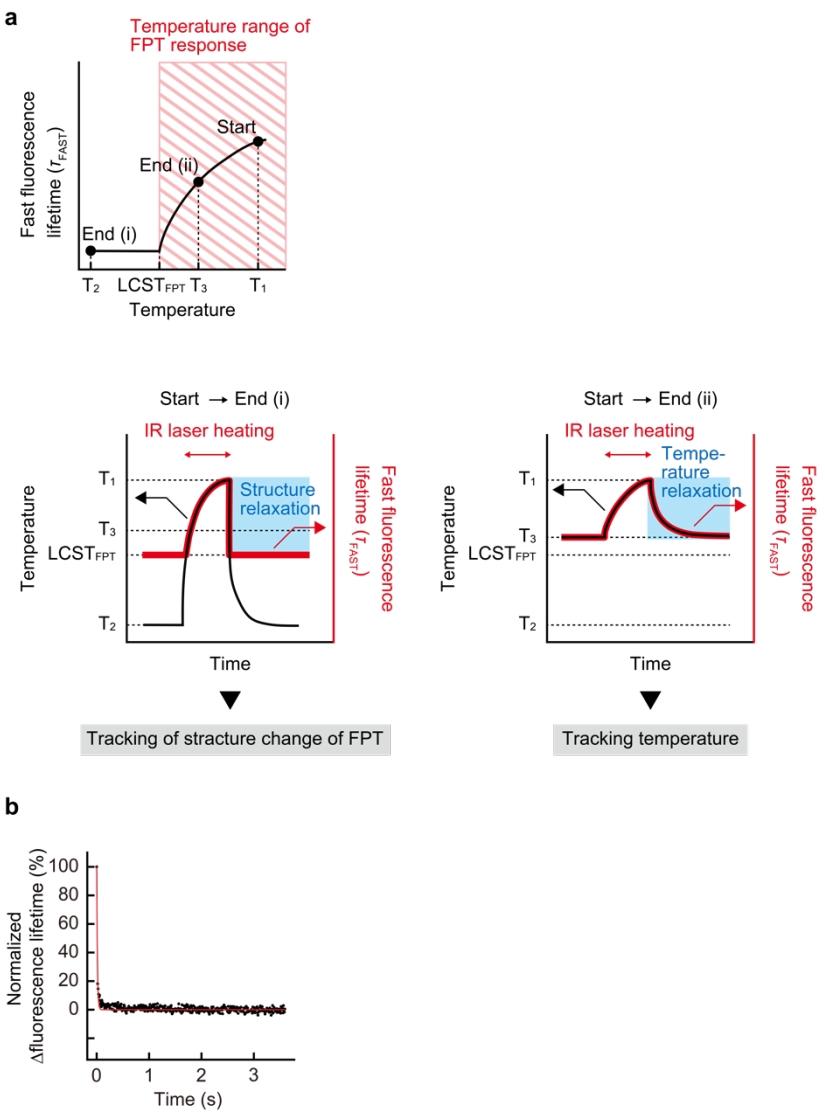

Supplementary Figure S6 | The Examination of time for structural change of FPT in living COS7 cells. a Schematic of this experiment. In principle, the temperature response dynamics of FPT includes both temperature and structural changes. FPT that changes its fluorescence lifetime due to the phase transition at temperatures above LCST does not respond at all below LCST (Upper panel). By lowering the base temperature before heating (T_2) below LCST, the response of FPT, which is sensitive only at temperatures above LCST, reflects structural relaxation (i, lower panel). On the other hand, when the base temperature before heating is set to T_3, which is higher than LCST, the fluorescence lifetime change reflects temperature (ii, lower panel). **b** The result for condition (i). The time required for FPT structural change was estimated by setting the temperature T_2 to a temperature (13 °C) that is significantly lower than the LCST of FPT (about 20 °C) to reduce the effect of temperature relaxation on the FPT fluorescence lifetime change. The red line shows an exponential approximation of the relaxation with a time constant of 13 ms.

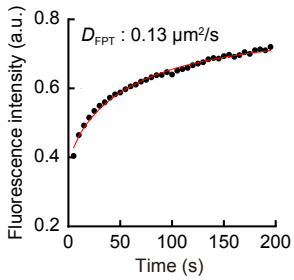

Supplementary Figure S7 | Molecular diffusion of FPT in living COS7 cells. Fluorescence recovery after photobleaching (FRAP) analysis of FPT. The recovery was fitted to the function by Soumpasis[38] (red line) to yield a diffusion constant (D_{FPT} = 0.13 $\mu m^2 s^{-1}$).

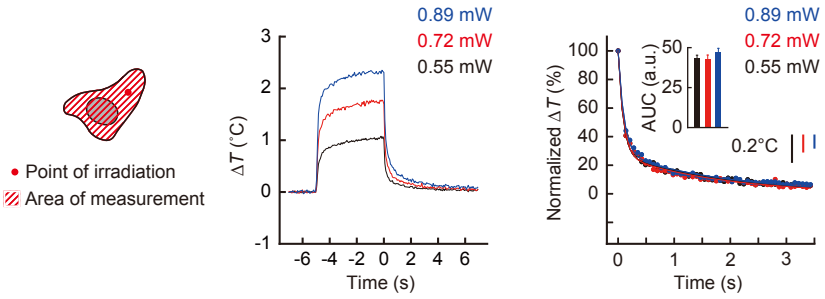

Supplementary Figure S8 | Independence of temperature increase (Δ*T*) on temperature relaxation rate. Tracking of the average temperature of whole cells when heated by continuous heating (5 s) with 0.55 (black), 0.72 (red), and 0.89 (blue) mW of IR laser irradiation (left). Normalized temperature relaxation of these three alternatives was compared (right). Scale bars represent indicated temperature changes. Data are presented as mean ± SE [n = 29 (0.55 mW), 30 (0.72 mW), 30 (0.89 mW) cells]. Inset in the right panel indicates area under the curve (AUC) of normalized temperature relaxation.

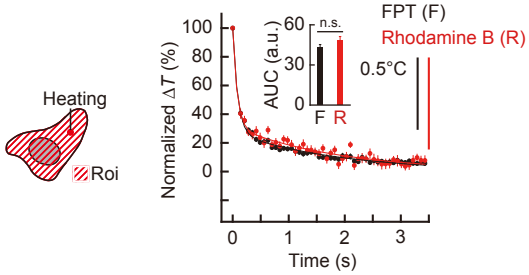

Supplementary Figure S9 | Monitoring of temperature relaxation with Rhodamine B in living COS7 cells. Comparison of normalized temperature relaxation after continuous heating with IR laser irradiation (5 s) between the result by FPT (black, Figure 3a) and that by Rhodamine B (IR laser: 0.55 mW, red). Scale bars represent indicated temperature changes. Data are presented as mean ± SE [n = 20 (Rhodamine B), 29 (FPT) cells]. Inset in the right panel indicates area under the curve (AUC) of normalized temperature relaxation. NS indicates not significant.

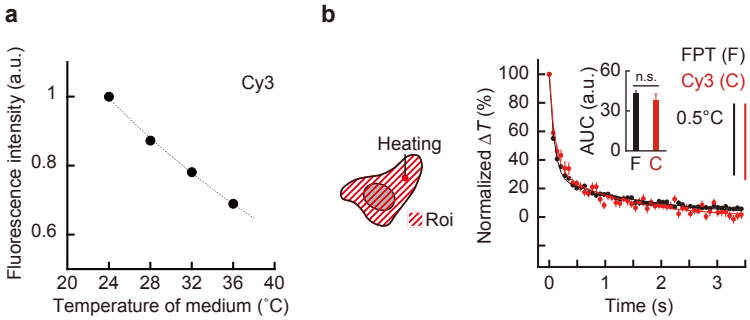

Supplementary Figure S10 | Monitoring of temperature relaxation with Cy3 in living COS7 cells. The temperature-dependent fluorescence intensity decrease (left). An exponential approximation (Fluorescence intensity $= 2.076e^{-0.0306T}$, where T indicates the temperature; $R^2 = 0.99$) was used for the estimation of temperature change (ΔT). Comparison of normalized temperature relaxation after continuous heating with IR laser irradiation (5 s) between the result by FPT (black, Figure 3a) and that by Cy3 (IR laser: 0.55 mW, red) (right). Scale bars represent indicated temperature changes. Data are presented as mean ± SE [n = 35 (Cy3), 29 (FPT) cells]. Inset in the right panel indicates area under the curve (AUC) of normalized temperature relaxation. NS indicates not significant.

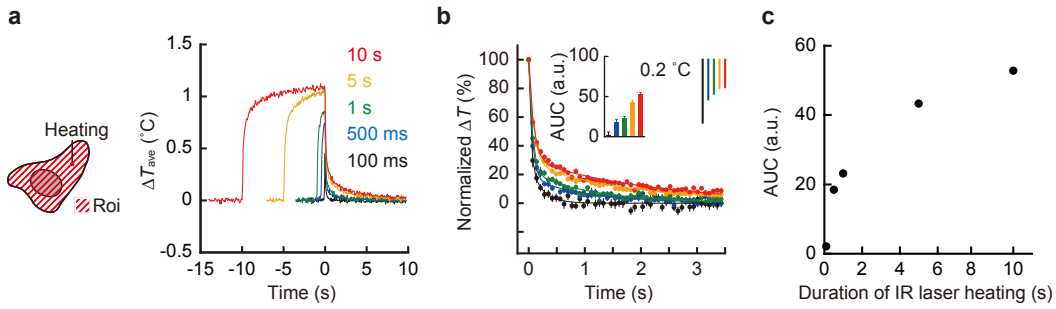

Supplementary Figure S11 | The dependency of the intracellular temperature relaxation rate on the heating duration. a Tracking of the average temperature of whole cells when heated with an IR laser (0.55 mW) for 10 s (red), 5 s (yellow), 1 s (green), 500 ms (blue), and 100 ms (black). **b** Normalized temperature relaxation of these five alternatives was compared. Data including the inset are mean ± s.e.m. [n = 30 (10 s), 29 (5 s), 30 (1 s), 30 (500 ms), and 28 (100 ms) cells]. Inset indicates area under the curve (AUC) of normalized temperature relaxation. Scale bars represent indicated temperature changes. **c** The relationship between the duration of heating and AUC of temperature relaxation.

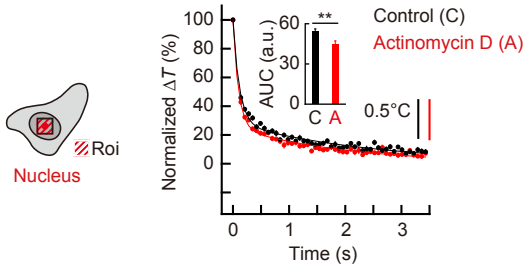

Supplementary Figure S12 | The effect of transcription inhibition on the rate of temperature relaxation in the nucleus of living COS7 cells. Normalized temperature relaxation of a square area with a 10 μm side centered on the heating point after continuous heating (IR laser: 0.55 mW for 5 s) in the nucleus was compared between untreated (control, black, Figure 3c) and Actinomycin D-treated (red) cells. Scale bars represent indicated temperature changes. Data are presented as mean ± SE (n = 30 cells). Inset indicates area under the curve (AUC) of normalized temperature relaxation. $^{**}P < 0.01$ (Welch's t test).

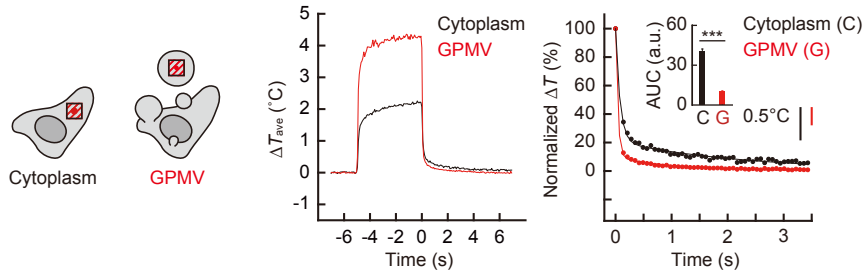

Supplementary Figure S13 | The comparison of temperature relaxation rate between the cytoplasm of living COS7 cells and their vesicles containing a portion of the cytoplasmic components. Tracking of the average temperature of a square area with a 10 μm side centered on the heating point when heated with an IR laser (0.55 mW) for 5 s in the cytoplasm (control, black, Figure 3c) and in GPMV (red) of COS7 cells (left). Normalized temperature relaxation of these two alternatives was compared (right). Scale bars represent indicated temperature changes. Data are presented as mean ± SE (n = 10 vesicles). Inset in the right panel indicates area under the curve (AUC) of normalized temperature relaxation. $^{***}P < 0.001$ (Welch's t test).

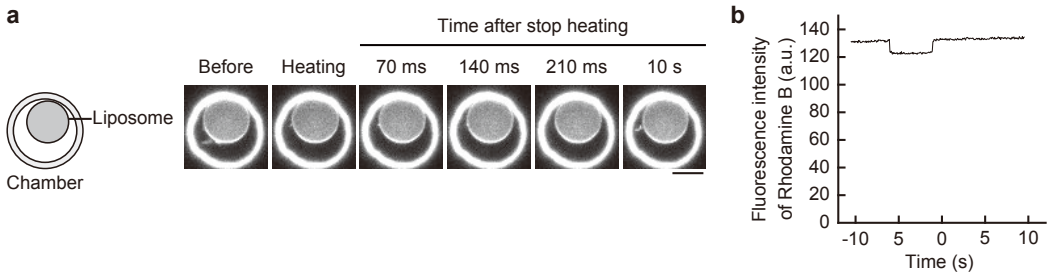

Supplementary Figure S14 | Tracking of temperature in liposomes during transient heating. a Fluorescence images of Rhodamine B in liposomes during heating (IR laser: 0.55 mW for 5 s). Liposomes were confined in a microchamber to prevent them from moving and disappearing from the field of view. The bright ring shape in the fluorescent images shows the structure of the chamber edge. Scale bar represent 10 μm. **b** Tracking temperature-dependent fluorescence intensity of Rhodamine B in liposomes.

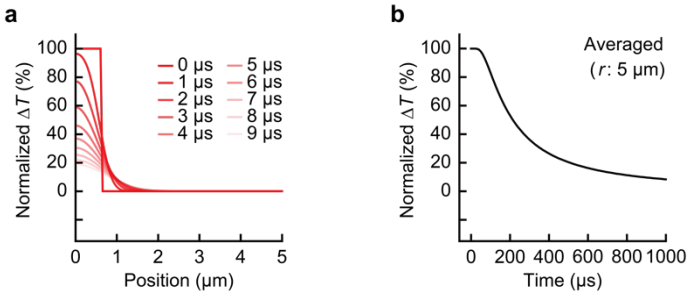

Supplementary Figure S15 | Time-course of temperature distribution after stopping heating numerically simulated with the heat conduction equation. a The temperature distribution after each time. **b** The relaxation of average temperature of an area of a 5 μm radius centered on the heating point. The numerical simulation was performed with the heat conduction equation (S3) and the thermal properties reported in cells (Supplementary Note 4).

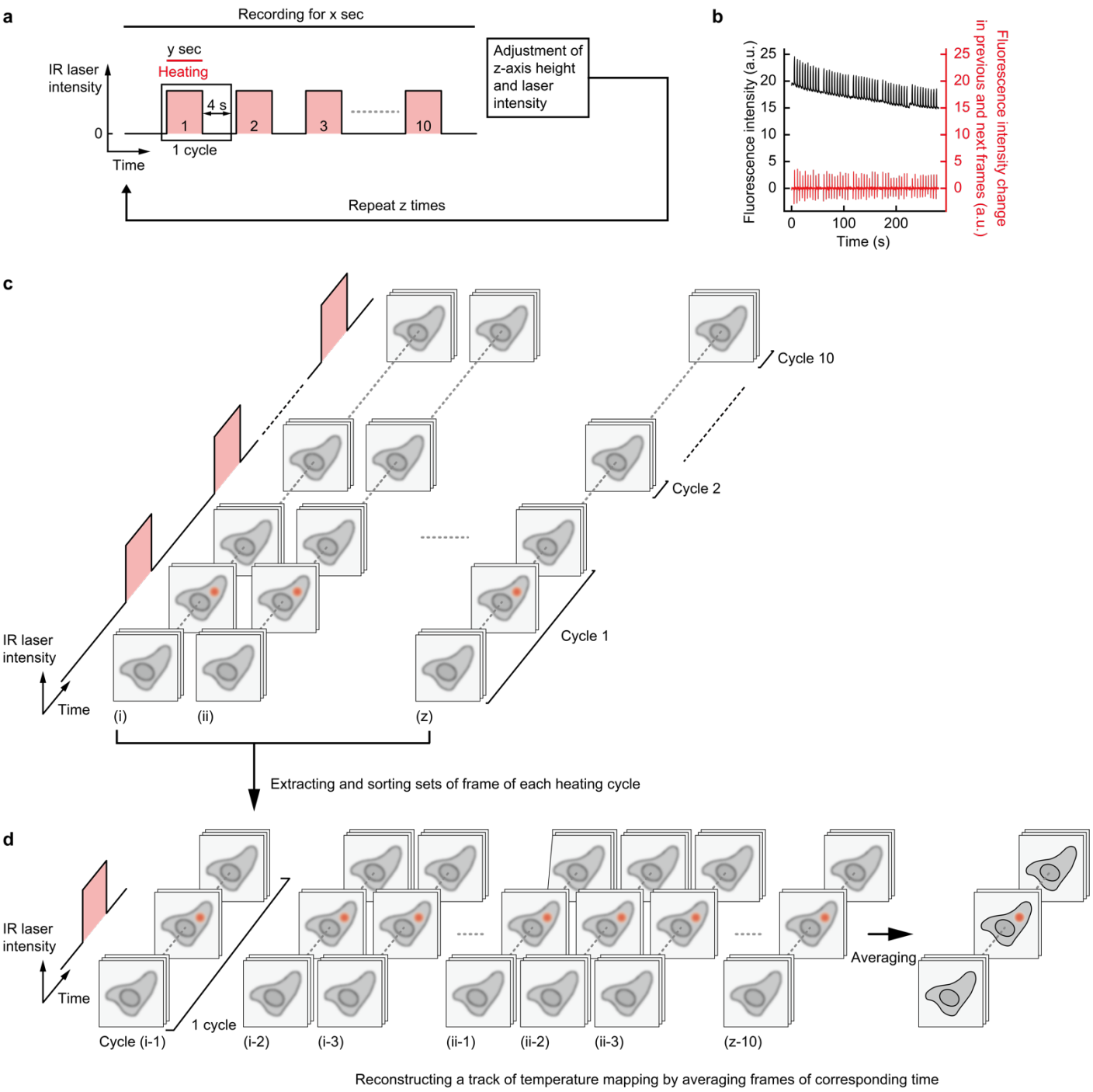

Supplementary Figure S16 | Tracking of intracellular temperature distribution upon IR laser heating. a Overview of imaging. Ten cycles of recording temperature relaxation for 4 s after y s of local heating in cells were repeated in continuous imaging for x s. **b** Time course of the fluorescence intensity in the field of view and the difference in fluorescence intensity between frames. **c** Video processing. The timing of heating stop was determined from the fluorescence intensity drop in b, and the subsequent time course of the fluorescence lifetime images was extracted for 4 s (one cycle). By averaging 10 × z movies for each cycle extracted from the continuous movie, a single high-resolution movie was reconstructed.

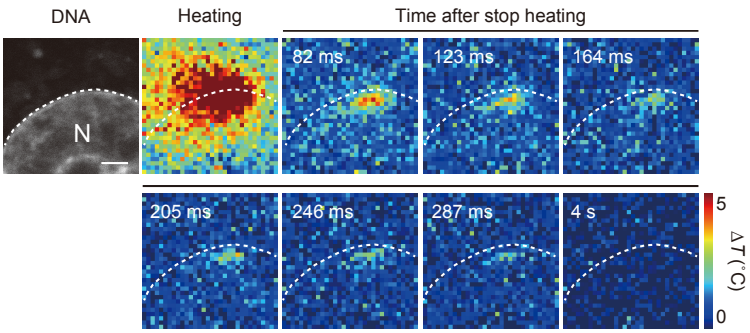

Supplementary Figure S17 | Simultaneous mapping of nuclear and cytoplasmic temperature relaxation. Real-time mapping of intracellular temperature immediately after stopping heating on the nuclear membrane (IR laser: 0.83 mW for 5 s). The nucleus was visualized with SiR-DNA. Scale bar represents 2 μm. Dotted line indicates the outline of the nucleus.

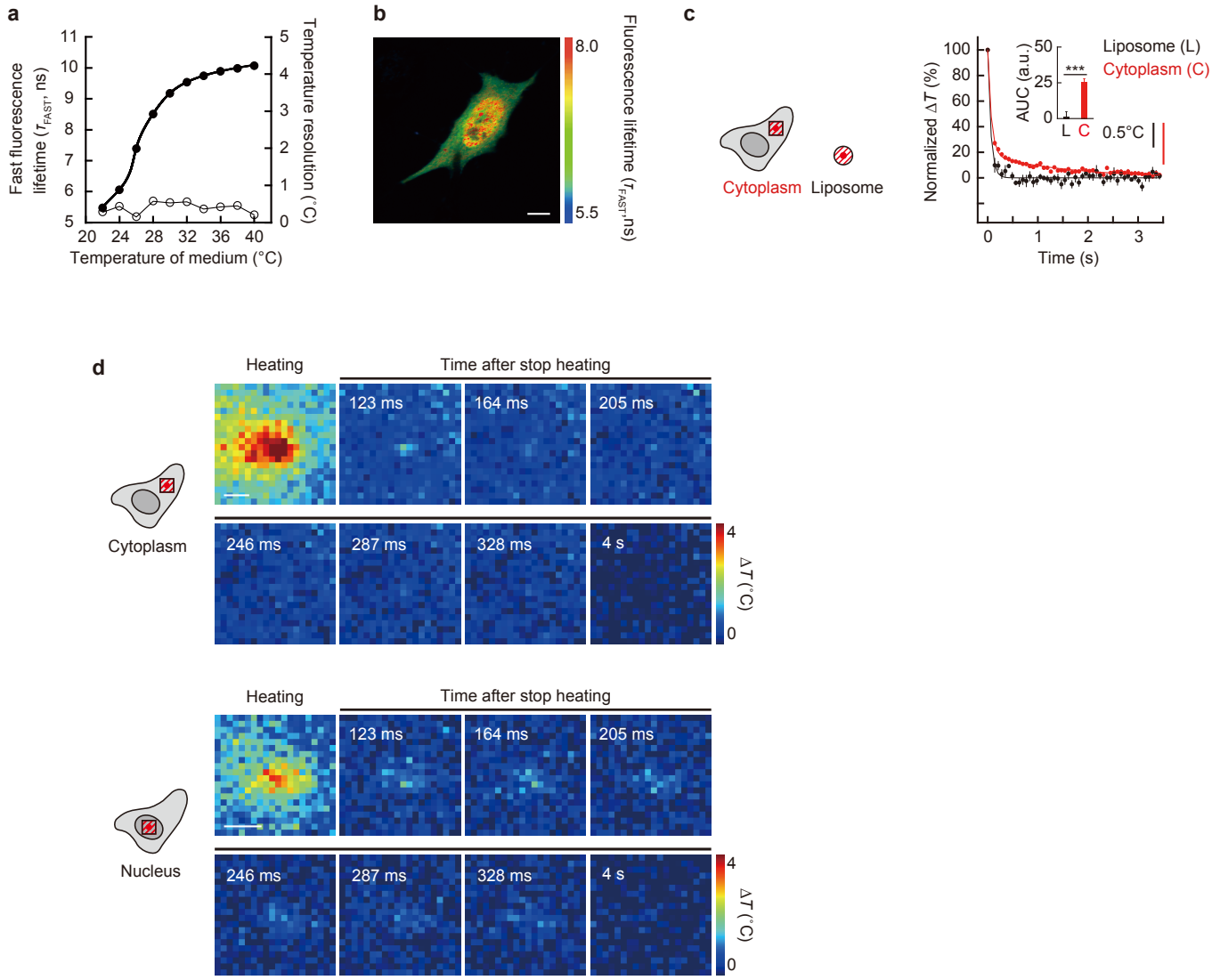

Supplementary Figure S18 | Real-time mapping of temperature in living HeLa cell. **a** The temperature response curve (closed, left axis) and temperature resolution (open, right axis) of FPT using fast fluorescence lifetime (τ_{FAST}). **b** Fluorescence lifetime (τ_{FAST}) images of FPT. Scale bar represents 10 µm. **c** Comparison of normalized temperature relaxation of liposome (Figure 3d, black) and that in a square area with a 10 µm side in living cells (red, IR laser: 0.55 mW) after the cessation of heating. Data are presented as mean ± SE [n = 10 (liposome), 28 (cytoplasm) cells]. Inset indicates area under the curve (AUC) of normalized temperature relaxation. $^{***}P < 0.001$ (Welch's t test). **d** Real-time mapping of intracellular temperature in the cytoplasm (upper panels) and in the nucleus (lower panels) immediately after stopping heating [0.83 mW (cytoplasm) and 0.55 mW (nucleus) for 5 s]. Scale bars represent 2 µm.

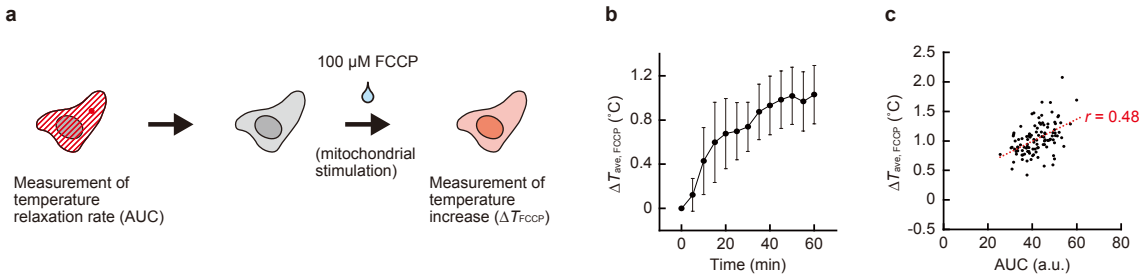

Supplementary Figure S19 | The relationship between the rate of intracellular temperature relaxation and the temperature increase in cells due to spontaneous heat generation. a Experimental Schematic. The AUC of normalized temperature relaxation was quantified by IR laser heating (0.55 mW, 5 sec), followed by tracking the average temperature change of whole cells when mitochondria were stimulated with FCCP (100 μM) in the same cells. **b** Time course of the average temperature change in cells (ΔT_{FCCP}) from immediately after the addition of FCCP. **c** The relationship between the AUC of normalized temperature relaxation and the temperature increase (ΔT_{FCCP}) in cells. The average temperature increase of whole cells at 60 min after the addition of FCCP in 109 cells is plotted as a function of the AUC of normalized intracellular temperature relaxation. The least-squares regression line is shown by the red dotted line ($\Delta T_{FCCP} = 0.0185\text{AUC} + 0.2533$, $r = 0.48$).

Supplementary Videos

Supplementary Video 1. Movie of Rhodamine B fluorescence inside single liposome upon heating with IR laser.

Supplementary Video 2. Movie of fluorescence lifetime of FPT inside single COS7 cell upon heating with IR laser.

Supplementary Video 3. Movie of fluorescence lifetime of FPT inside single COS7 cell upon heating for 5 s with IR laser.

Supplementary Video 4. Movie of fluorescence lifetime of FPT inside single COS7 cell upon heating for 1 s with IR laser.

Supplementary Video 5. Movie of fluorescence lifetime of FPT inside single COS7 cell upon heating for 500 ms with IR laser.

Supplementary Video 6. Movie of fluorescence lifetime of FPT in the cytoplasmic region of COS7 cells upon heating with IR laser.

Supplementary Video 7. Movie of fluorescence lifetime of FPT in the nuclear region of COS7 cells upon heating with IR laser.

Supplementary References

41. Lervik, A., Bresme, F., Kjelstrup, S., Bedeaux, D. & Rubi, J. M. Heat transfer in protein–water interfaces. *Phys. Chem. Chem. Phys.* **12**(7), 1610–1617 (2010).

42. Bastos, A. R. *et al.* Thermal properties of lipid bilayers determined using upconversion nanothermometry. *Adv. Funct. Mater.* **29**(48), 1905474 (2019).

43. Giering, K., Lamprecht, I., Minet, O. & Handke, A. Determination of the specific heat capacity of healthy and tumorous human tissue. *Thermochimica Acta* **251**, 199–205 (1995).

44. Bryan, A. K. *et al.* Measuring single cell mass, volume, and density with dual suspended microchannel resonators. *Lab. Chip.* **14**, 569–576 (2014).

45. Hong, S., *et al.* Sub-nanowatt microfluidic single-cell calorimetry. *Nat. Commun.* **11**, 2982 (2020).